nanomaterials

MDPI

Article

Photoinduced Glycerol Oxidation over Plasmonic Au and AuM (M = Pt, Pd and Bi) Nanoparticle-Decorated TiO_2 Photocatalysts

Trin Jedsukontorn [1], Nagahiro Saito [2] and Mali Hunsom [1,3,4,*]

1 Fuels Research Center, Department of Chemical Technology, Faculty of Science, Chulalongkorn University, Bangkok 10330, Thailand; Trinatabo_jed@hotmail.com
2 Graduate School of Engineering & Green Mobility Collaborative Research Center, Nagoya University, Nagoya 464-8603, Japan; hiro@sp.material.nagoya-u.ac.jp
3 Center of Excellence on Petrochemical and Materials Technology (PETRO-MAT), Chulalongkorn University, Bangkok 10330, Thailand
4 Associate Fellow of Royal Society of Thailand (AFRST), Sanam Suea Pa, Dusit, Bangkok 10300, Thailand
* Correspondence: mali.h@chula.ac.th; Tel.: +66-(2)-218-7523-5; Fax: +66-(2)-255-5831

Received: 26 March 2018; Accepted: 19 April 2018; Published: 23 April 2018

Abstract: In this study, sol-immobilization was used to prepare gold nanoparticle (Au NP)-decorated titanium dioxide (TiO_2) photocatalysts at different Au weight % (wt. %) loading (Au_x/TiO_2, where x is the Au wt. %) and Au–M NP-decorated TiO_2 photocatalysts (Au_3M_3/TiO_2), where M is bismuth (Bi), platinum (Pt) or palladium (Pd) at 3 wt. %. The Au_x/TiO_2 photocatalysts exhibited a stronger visible light absorption than the parent TiO_2 due to the localized surface plasmon resonance effect. Increasing the Au content from 1 wt. % to 7 wt. % led to increased visible light absorption due to the increasing presence of defective structures that were capable of enhancing the photocatalytic activity of the as-prepared catalyst. The addition of Pt and Pd coupled with the Au_3/TiO_2 to form Au_3M_3/TiO_2 improved the photocatalytic activity of the Au_3/TiO_2 photocatalyst by maximizing their light-absorption property. The Au_3/TiO_2, Au_3Pt_3/TiO_2 and Au_3Pd_3/TiO_2 photocatalysts promoted the formation of glyceraldehyde from glycerol as the principle product, while Au_3Bi_3/TiO_2 facilitated glycolaldehyde formation as the major product. Among all the prepared photocatalysts, Au_3Pd_3/TiO_2 exhibited the highest photocatalytic activity with a 98.75% glycerol conversion at 24 h of reaction time.

Keywords: glycerol conversion; gold nanoparticles; metal decorated TiO_2; bimetallic nanoparticles; photocatalytic oxidation

1. Introduction

Biodiesel has recently become a globally attractive renewable biomass energy source. The increasing production of biodiesel has led to glycerol, the inevitable by-product from the biodiesel production process, becoming oversupplied in the market. To capitalize on the economic aspect of biodiesel production, it is essential to contrive a process for using glycerol in more valuable products. Due to the highly functionalized chemical molecule of glycerol, it is a potential bio-platform molecule that can be converted into viable chemicals and intermediate products for the chemical industry through a range of catalytic routes, such as fermentation [1], dehydrogenation [2], dehydration [3], etherification [4], esterification [5] and oxidation [6]. Consequently, the valorization of biodiesel-derived glycerol has gained much attention for increasing the proficiency and economic viability of the use of biomass resources. Among a large number of effective processes for glycerol transformation, aerobic oxidation is one of the extensively studied routes, since it can promote

the generation of high-value fine chemicals and useful intermediates in organic synthesis, such as glycolic acid (GCOA), glyceric acid (GCA), glyceraldehyde (GCD), and dihydroxyacetone (DHA) [6,7]. However, the major hindrance in the glycerol oxidation process at a commercial scale is its requirement for an alkaline condition, high operating temperature and pressure, and the deactivation of the utilized catalyst. Thus, there is an urgent need to find a new, green process to address the increasing demands of sustainable and clean-energy technologies. In the last two decades, photocatalytic technology has been regarded as one of the most attractive processes due to its superior features, such as being environmentally benign, high efficiency, and operation at room temperature and atmospheric pressure. Many researchers have focused on this process, with versatile applications ranging from the field of wastewater and air remediation [8,9], carbon dioxide (CO_2) reduction [10], clean hydrogen (H_2) production [11] and the synthesis of high-value organic compounds [12], towards the development of an efficient solar-to-energy conversion [13].

A wide spectrum of semiconductors, such as TiO_2, bismuth(III) oxide (Bi_2O_3), zinc oxide (ZnO), silicon carbide (SiC), tungsten(VI) oxide (WO_3) and carbon nitride (C_3N_4), have been explored for their use in photocatalytic processes. Among all the commercial photocatalysts, TiO_2 has the greatest appeal as a benchmark material in the fields of environmental remediation and solar fuel production, and still remains the most efficient and suitable material for light-energy harvesting. This is due to its many positive features, such as excellent photo-stability, high conductivity, low toxicity, low price and corrosion resistance. Despite these advantages, TiO_2 is only optically active in the ultraviolet (UV) light region (~5% of the total solar spectrum), and together with the rapid recombination rate of photo-induced charge carriers. These are the main barriers that make TiO_2 industrially less attractive. Several approaches to improve the photocatalytic performance of TiO_2 nanostructures have been explored. The loading of TiO_2 with a co-catalyst, such as metal nanoparticles (NPs) or secondary narrowed-bandgap semiconductors, to act as an electron-sink in order to boost the quantum yield is a promising effective approach. In addition, the decoration of metal NPs can also provide active sites for the reaction and alter the adsorption behavior of molecules by changing their polarizability, among other properties, leading to the preferential generation of the desired value-added products [14]. Various plasmonic noble metal NP-decorated TiO_2 nanostructures that enhance the generation and migration of hot electrons from the metal to TiO_2 have been widely reported [15–17]. Among all the decorated metal co-catalysts, Au has been found to be the most active metal, which is attributed to its noble nature, i.e., visible light active arising from the collective coherent oscillation of surface electrons through localized surface plasmon resonance (LSPR) [18–22], its low susceptibility to oxygen, high chemical stability [23] and effective charge transfer from TiO_2 to it and/or *vice versa* [24]. The synthesis of Au NPs has become of great interest in recent decades. The most impressive technique for AuNP synthesis is the two-phase reduction method developed by Brust and co-workers [25,26]. The breakthrough for using Au NPs as a heterogenous catalyst has occurred since Haruta and Hutching provided the significant observations that Au NPs was very active for CO oxidation and ethylene hydrochlorination [27,28]. Apart from that, to date many reports have pointed out that Au NPs are also active in a range of catalytic routes such as glycerol conversion [7,29,30], water splitting [20,31], H_2 generation [21,32], the photo-oxidation of organic substrates [22,33–35] and the photo-reduction of organic compounds [36,37].

Besides the monometallic Au, the combination of Au NPs with other metals can enable an enhanced global reaction system and promote the desired reaction pathway depending on their structural and/or electronic properties at the nanoscale level. Bimetallic Au-based NPs have been studied in a variety of reactions, including solvent-free benzyl alcohol oxidation to benzaldehyde [38]; selective oxidation of methanol to methyl formate [39]; photocatalytic H_2 production from ethanol reforming over core–shell Au-palladium (Pd) promoters [40] and over bimetallic Au-platinum (Pt) NPs [41]; selective oxidation of furfural to furoic acid [42]; selective oxidation of 1,2-propanediol to lactic acid [43]; selective oxidation of ethanol to acetaldehyde [44]; and the degradation of ciprofloxacin [45]. Apart from these reactions, glycerol oxidation in a liquid phase system has also been

intensively investigated over a bimetallic Au-based system [46–49]. The synergism between Au and a coupled metal (e.g., Pt or Pd) can boost up the glycerol conversion and tune the selectivity of oxidation products. Moreover, the synthesis procedure and particle size of as-prepared bimetallic Au-based NPs also significantly affected the product distribution and route of glycerol transformation [47,50,51].

As far as we know, there have been only a few research reports on the photocatalytic oxidation of glycerol over metal-decorated TiO_2. Panagiotopoulou et al. [52] prepared Pt impregnated on TiO_2 and utilized the prepared Pt/TiO_2 for the photo-reforming and photo-oxidation of glycerol. The Pt/TiO_2 photocatalyst exhibited a more efficient reaction rate for glycerol oxidation than bare TiO_2, which was mainly due to the increased separation of the charge carriers and the elevation of the rate-limiting cathodic half reaction (oxygen (O_2) reduction) in the glycerol photo-oxidation. Likewise, the addition of any of Bi, Au, Pt or Pd on TiO_2 was reported in our previous work to further enhance the rate of glycerol photo-oxidation, where Au-decorated TiO_2 exhibited the best performance [53]. However, the photocatalytic conversion of glycerol over the surface of metals and metal oxides to the desired products still requires a thorough comprehension of the surface chemistry and reaction mechanism. The bias towards certain reaction pathways can be modulated by varying the reaction conditions (light, pressure, temperature, etc.), reaction media (water with O_2 or hydrogen peroxide) and the nature of the catalyst surface (i.e., monometal, bimetal and/or metal oxide). Thus, in this work, we investigated the photocatalytic oxidation of glycerol over Au-based mono- and bimetallic NP-decorated TiO_2. The aim was to explore the individual as well as the combined effects of Au, Au-Bi, Au-Pt and Au-Pd on the photocatalytic performance of TiO_2 for the photocatalytic oxidation of glycerol. The Bi, Pt and Pd NPs were selected to combine with Au because Bi prefers to react with the secondary hydroxyl group of glycerol to form DHA while the Pt and Pd can promote the activity of glycerol oxidation [53–56].

2. Experiment

2.1. Preparation of the Au/TiO$_2$ and AuM/TiO$_2$ Photocatalysts

Both mono- and bimetallic NP-decorated TiO_2 photocatalysts were prepared by sol-immobilization, which has been previously reported to be an outstanding preparation method [51,57]. Commercial TiO_2 powder (Sigma Aldrich, St. Louis, MO, USA) containing ≥99% anatase phase structure was used as the support semiconductor material. The Au NP-decorated TiO_2 (Au/TiO_2) at different Au contents from 1 wt. % to 7 wt. % were prepared using sodium borohydride ($NaBH_4$; Loba Chemie, Mumbai, India) as a reducing agent. In brief, for the 1 wt. % Au NP-decorated TiO_2 (Au_1/TiO_2), 40.8 mg of $HAuCl_4 \cdot 3H_2O$ (Sigma Aldrich) was dissolved in deionized (DI) water. Then, 2 wt. % polyvinyl alcohol (PVA; $[-CH_2CHOH-]_n$, 99% hydrolyzed, Sigma Aldrich) was added to a 1:10 molar ratio of PVA: $HAuCl_4 \cdot 3H_2O$ with stirring at a constant rate of 300 rpm in order to stabilize the metal dispersion on the support and prevent agglomeration. Next, 1.98 g of TiO_2 (Anatase, Sigma Aldrich) was added to the prepared solution and then excess $NaBH_4$ was slowly added to the colloidal solution. The reaction was held for 24 h at atmospheric pressure and temperature to obtain the complete sol immobilization. The obtained mixture was filtered and washed thoroughly several times with DI water until no chloride ions remained, which was detected in the filtrate solution by the silver nitrate test. Finally, the obtained solid was dried at 110 °C in a hot air oven overnight and, subsequently, the organic scaffold residue was removed and the catalyst was activated by heat treatment under a N_2 flow at 350 °C for 3 h followed by a H_2 flow at 350 °C for 3 h, respectively, to yield the ready-to-use Au_1/TiO_2. A similar procedure was repeated for the 3, 5 and 7 wt. % Au NP-decorated TiO_2, except using 122.45, 204.06 and 285.72 mg of $HAuCl_4 \cdot 3H_2O$ instead of 40.8 mg to yield the Au_3/TiO_2, Au_5/TiO_2 and Au_7/TiO_2 photocatalysts, respectively.

To prepare the Au-based bimetallic NP-decorated TiO_2 photocatalysts with a 3 wt. % loading of both Au and the selected metal NPs (Au_3M_3/TiO_2), three types of second metal (Bi, Pt, and Pd) were separately incorporated with the Au on TiO_2 to yield the Au_3Bi_3/TiO_2, Au_3Pt_3/TiO_2 and Au_3Pd_3/TiO_2 photocatalysts, respectively, via the same method. For the Au_3Bi_3/TiO_2 photocatalyst, 122.45 mg of

$HAuCl_4 \cdot 3H_2O$ was dissolved in 10 mL of DI water, while 90.9 mg of bismuth(III) chloride ($BiCl_3$; Sigma Aldrich) was dissolved in 10 mL of 0.2 M of hydrochloric acid (HCl; 37% purity, Sigma Aldrich). Both solutions were mixed together and added to 10.5 mL of 2 wt. % PVA with stirring at constant rate of 300 rpm in order to stabilize the metal dispersion on the support and prevent agglomeration. Then, 1.88 g of TiO_2 was added to the prepared solution and subsequently reduced by the slow addition of $NaBH_4$ to get the colloid solution. The reaction was held for 24 h to obtain complete sol immobilization. Then, the obtained mixture was filtered and washed thoroughly with DI water until no chloride ions. Finally, the obtained solid was dried in an oven and subsequently removed the organic scaffold residue and activated by heat treatment under a N_2 flow followed by a H_2 flow as above to yield the ready-to-use Au_3Bi_3/TiO_2. Similar procedures were repeated for the synthesis of the Au_3Pt_3/TiO_2 and Au_3Pd_3/TiO_2 photocatalysts except using 159.6 mg of chloroplatinic acid hexahydrate ($H_2PtCl_6 \cdot 6H_2O$; Sigma Aldrich) dissolved in 10 mL of DI water and 100 mg of palladium (II) chloride ($PdCl_2$; Sigma Aldrich) solution dissolved in 10 mL of 0.2 M HCl instead of the $BiCl_3$.

2.2. Characterization of the as-Prepared Au_x/TiO_2 and Au_3M_3/TiO_2 Photocatalysts

The diffractogram peaks of all prepared photocatalysts were first characterized by X-ray diffraction (XRD) using a D8 Discover-Bruker AXS X-ray diffractometer (Billerica, MA, USA) equipped with Cu Kα in order to evaluate the crystal and phase structure. The X-ray diffractometer was operated at 40 mA and 40 kV with acquiring step of 0.02° between angles of 10–80 degrees. The diffractogram peaks were identified using the JCPDS database. The loading content of the decorated metal on the TiO_2 surface was examined by scanning electron microscopy (SEM; JSM-6610LV) (Peabody, MA, USA) equipped with energy-dispersive X-ray spectrometry (EDS) to perform elemental analysis at the atomic resolution. The dispersion of decorated-metals and particle size distribution were observed by transmission electron microscopy (TEM; JEOL-2100Plus, Tokyo, Japan) at an electron acceleration of 200 kV. Elemental line scan and mapping of the decorated metal were also observed on a JEOL 2100 Plus equipped with a Bruker EDS using a nominal electron beam size of 1 nm. The average metal particle sizes and their distribution were calculated by averaging not less than 100 particles randomly distributed in the TEM images. The diffuse reflectance spectra were monitored via UV-visible near infrared spectrometry (UV-Vis-NIR; Perkin Elmer, Lambda 950, Waltham, MA, USA) over a wavelength of 320–820 nm. The elemental oxidation states of all the prepared photocatalysts were assessed by X-ray photoelectron spectroscopy (XPS; PHI 5000 VersaProbeII) (ULVAC-PHI, Inc., Kanagawa, Japan) with a monochromatized Al Kα source (hν = 1486.6 eV). Accurate binding energies ($\pm$0.1 eV) were established with respect to the position of the adventitious carbon C1s peak at 284.8 eV. The spectra deconvolution was performed using the XPSPEAK41 software package (Kratos Analytical Ltd., Manchester, UK).

2.3. Photocatalytic Activity Test

The photocatalytic activity of all the prepared photocatalysts was tested via the photocatalytic oxidation of glycerol at room temperature and ambient pressure using a 120 W high-pressure mercury lamp (RUV 533 BC, Holland, The Netherlands) at light intensity 4.7 mW/cm^2. The photoreactor was placed in the middle of a UV-protected box (0.68 m $\times$ 0.68 m $\times$ 0.78 m) containing 100 mL of 0.3 M glycerol (QReC). The solution was agitated at 300 rpm to achieve complete mixing. Oxygen was supplied continuously into the reactor at a constant feed rate of 200 mL/min. Prior to light illumination, the selected photocatalyst was suspended in the glycerol solution in a dark room for 30 min to reach an adsorption equilibrium. As the experiment progressed, 2 mL of sample was collected and then centrifuged on a KUBOTA KC-25 digital laboratory centrifuge (KUBOTA, Tokyo, Japan) to separate the solid catalyst from the aqueous product. The variation in the glycerol concentration and the generation of all monitored compounds, including GCD, DHA, hydroxypyruvic acid (HPA), GCOA, formaldehyde (FMD) and glycolaldehyde (GCAD), were analyzed by high-performance liquid chromatography with a RID-10A refractive index detector (Shimadzu, LC-10 ADVP, Kyoto, Japan). The stationary phase was an Aminex HPX-87H ion-exclusion column (300 $\times$ 7.8 mm), and the mobile phase

was a 70:30 (v/v) water: acetonitrile solution in 0.5 mM H_2SO_4 at a constant flow rate of 0.4 mL/min. Standard solutions of glycerol, GCD (Sigma Aldrich), DHA (Merck, Kenilworth, NJ, USA), HPA (Sigma Aldrich), GCA (Ajax Finechem, Taren Point, Australia), FMD (Merck), GCOA (Ajax Finechem) and GCAD (Sigma Aldrich) were run to identify the retention times and determine the relationships between the peak area and concentration. The conversion of glycerol (X) and yield (Y) of each selected product of the photocatalytic oxidation were calculated according to Equations (1) and (2), respectively:

$$X(\%) = \frac{\text{Amount of glycerol converted (C} - \text{based mole)}}{\text{Total amount of glycerol in reactant (C} - \text{based mole)}} \times 100 \quad (1)$$

$$Y(\%) = \frac{\text{Amount of glycerol converted to product } j \text{ (C} - \text{based mole)}}{\text{Total amount of glycerol in reactant (C} - \text{based mole)}} \times 100 \quad (2)$$

3. Results and Discussion

3.1. Au/TiO$_2$ Photocatalysts

3.1.1. Photocatalyst Morphology

Representative XRD patterns of the as-synthesized Au_x/TiO_2 photocatalysts with different metal loading contents are displayed in Figure 1a. All photocatalysts exhibited the main diffraction peaks of TiO_2 in the anatase phase at a 2θ of 25.3°, 37.0°, 37.9°, 38.6°, 48.1°, 53.9°, 55.1°, 62.7°, 68.8°, 70.3° and 75.1°, corresponding to the (101), (103), (004), (112), (200), (105), (221), (204), (116), (220) and (215) crystal planes, respectively (JCPDS No. 21-1272), with an additional rutile peak in trivial content at 27.5° corresponding to the (101) crystal plane (JCPDS No. 04-0802) (Figure 1a$_1$). In addition, the diffraction peaks of Au NPs appeared at about 38.2°, 44.4°, 64.6° and 77.6°, assigning to the face-centered cubic structure of Au with (111), (200), (220) and (311) planes (JCPDS No. 002-1095), indicating the presence of metallic Au in the as-synthesized Au_x/TiO_2 photocatalysts. The intensity of the Au peaks increased as the content of Au decorated on the TiO_2 surface increased, but without a shift in the peak position (Figure 1a$_2$,a$_3$).

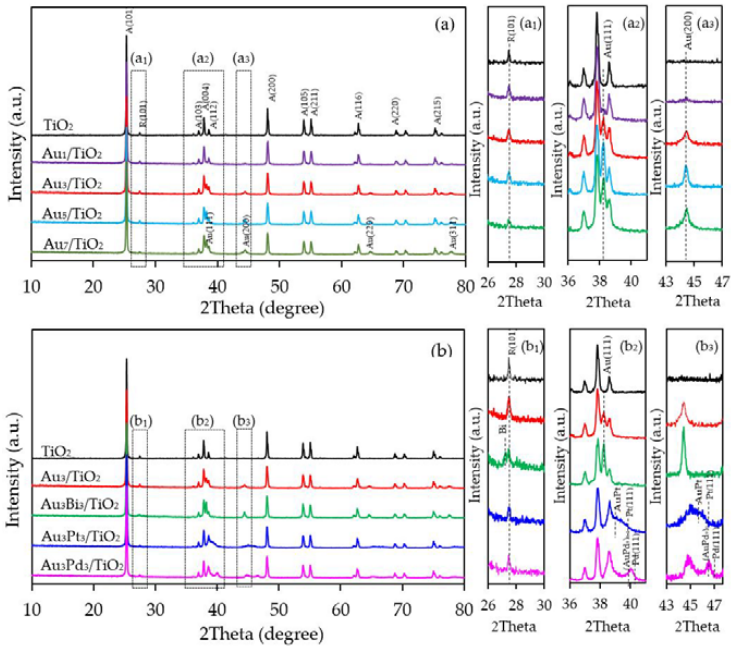

Figure 1. Representative X-ray diffraction (XRD) patterns of the (**a**) Au_x/TiO_2 and (**b**) Au_3M_3/TiO_2 photocatalysts.

The qualitative presence of Au in all the Au_x/TiO_2 photocatalysts was also confirmed by SEM–EDS analysis (Figure 2). Quantitatively, as summarized in Table 1, the Au content in each Au_x/TiO_2 photocatalyst was close to the set value. The TEM images of the as-prepared photocatalysts with the derived Au NPs size distribution are displayed in Figure 3. They exhibited well-dispersed decorated Au NPs on the TiO_2 surface with a narrow size distribution. The average size of Au NPs increased slightly as the Au content increased, suggesting an agglomeration of Au NPs in the presence of a high Au loading content.

Table 1. Properties of the as-synthesized Au_x/TiO_2 and Au_3M_3/TiO_2 photocatalysts.

Photocatalyst	Au Loading (wt. %) [a]	M Loading (wt. %) [a]	Decorated Metal Particle Size (nm) [b]	Bandgap Energy (eV) [c]	Ti^{3+}/Ti^{4+} [d]
Au_1/TiO_2	0.98 ± 0.10	n.d.	6.36 ± 0.75	3.00	0.1220
Au_3/TiO_2	3.02 ± 0.21	n.d.	6.69 ± 0.86	3.00	0.1478
Au_5/TiO_2	4.96 ± 0.19	n.d.	10.04 ± 1.11	2.94	0.2198
Au_7/TiO_2	7.08 ± 0.35	n.d.	10.84 ± 1.01	2.80	0.2412
Au_3Bi_3/TiO_2	2.96 ± 0.12	3.11 ± 0.28	11.84 ± 1.11	2.85	0.1960
Au_3Pt_3/TiO_2	3.06 ± 0.10	3.01 ± 0.20	7.61 ± 0.91	2.85	0.1941
Au_3Pd_3/TiO_2	3.09 ± 0.14	3.05 ± 0.22	9.66 ± 1.06	2.79	0.3561

[a] Estimated from the scanning electron microscopy–energy-dispersive X-ray spectrometry (SEM–EDS) analysis; [b] Average (± standard deviation (SD)) metal particle size obtained from the transmission electron microscopy (TEM) analysis; [c] Calculated from Tauc's plot (plot of $(\alpha h\nu)^{1/n}$ against $(h\nu)$); [d] Calculated from area under deconvoluted high-resolution X-ray photoelectron spectroscopy (HR-XPS) peak of Ti2p; n.d., not detected.

Figure 4a exhibits the UV-vis absorption spectra of the Au_x/TiO_2 photocatalysts with different Au contents. The parent TiO_2 exhibited the main intense UV absorption band at a wavelength of less than 400 nm with no absorption band in the visible light region or at a wavelength of greater than 400 nm. This was mainly due to its large bandgap energy that enabled the electron transfer from the filled valence O 2p orbitals of the valence band to the vacant Ti 3d orbitals of the conduction band only by the excitation of the photon energy from the UV light region. However, all the Au_x/TiO_2 photocatalysts exhibited an enhanced visible light absorption with an intense broad absorption band centered at wavelength around 540 nm. The peak intensity increased as the Au content increased from 1.0 wt. % to 7.0 wt. %. The presence of the visible light absorption of all Au_x/TiO_2 photocatalysts might be caused by the LSPR effect of the decorated Au NPs that can absorb visible light through the polarization and oscillation of the conduction electrons in the metal structure [58]. However, as reported previously, the LSPR band of well-dispersed spherical Au nanocrystals is generally sharp and appears at a wavelength of 520 nm [59]. The absorption center of all the prepared Au_x/TiO_2 photocatalysts in this study deviated from the mentioned wavelength (520 nm) with a broad tail extending towards longer wavelengths, which might be attributed to the anisotropy of the trigonal/prismatic shape (non-spherical) of the Au nanocrystals [60]. The bandgap values of all samples were determined from a Tauc's plot (inset of Figure 4a), and are listed in Table 1. The addition of Au NPs at 1 and 3 wt. % affected insignificantly the bandgap energy of the parent TiO_2. In that, both contents decreased the bandgap value of TiO_2 from 3.02 eV to 3.0 eV, probably because both low Au contents can induce only a small formation of Ti^{3+} defect structure which cannot intensely alter the major electronic state position of the O2p valence orbital as well as the localized band bending of the O2p valence band edge maximum. However, addition of Au NPs at loading of 5 and 7 wt. % importantly decreased the band-gap value of TiO_2 to 2.94 and 2.80 eV, respectively. This indicated that the presence of a high defective TiO_2 structure in the presence of high Au content (5 and 7 wt. %) can alter the major electronic state of the valence band and conduction band position.

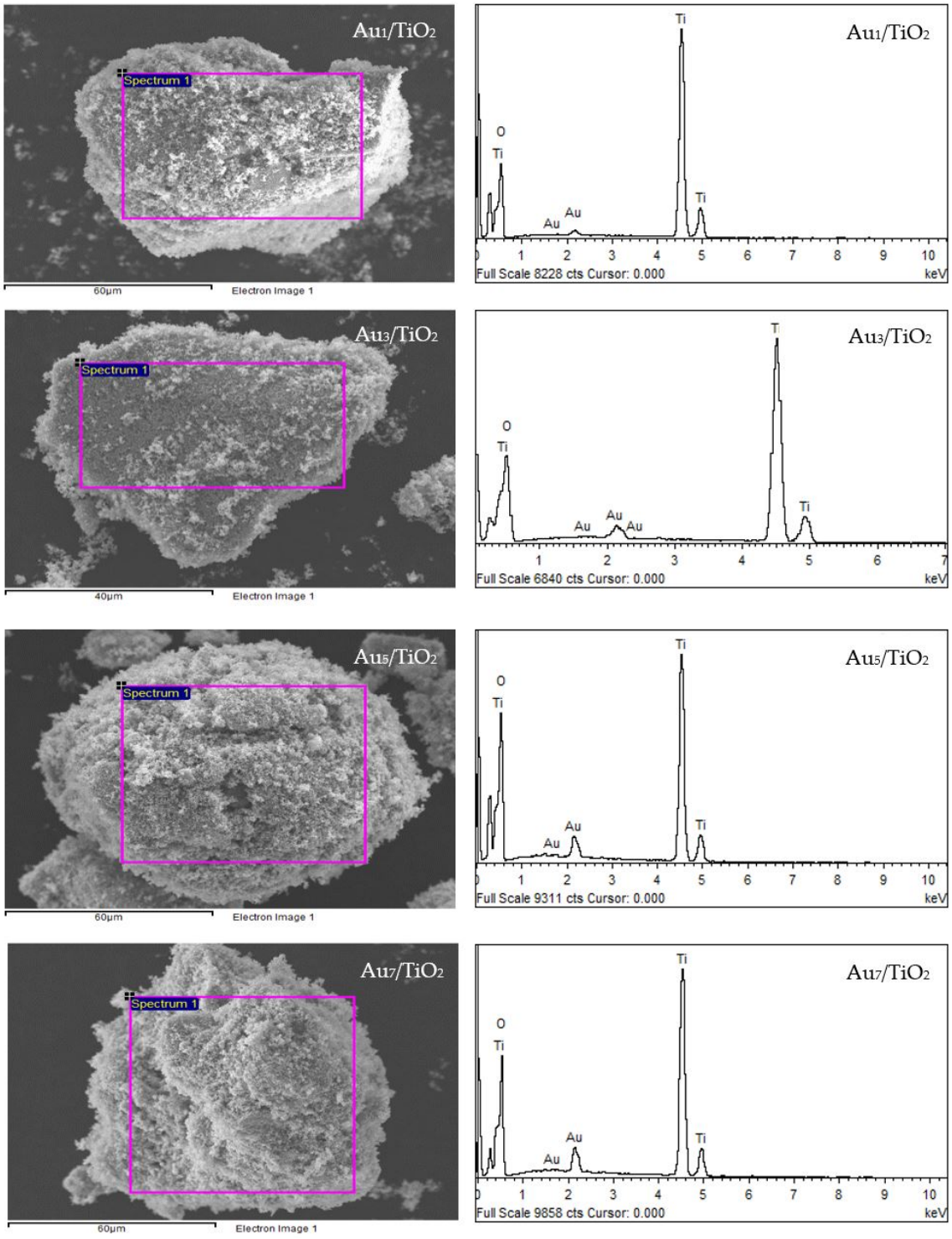

Figure 2. (**Left**) Representative SEM images of the different Au_x/TiO_2 photocatalysts and (**Right**) the EDS elemental analysis of the corresponding area shown in the rectangle on the SEM image.

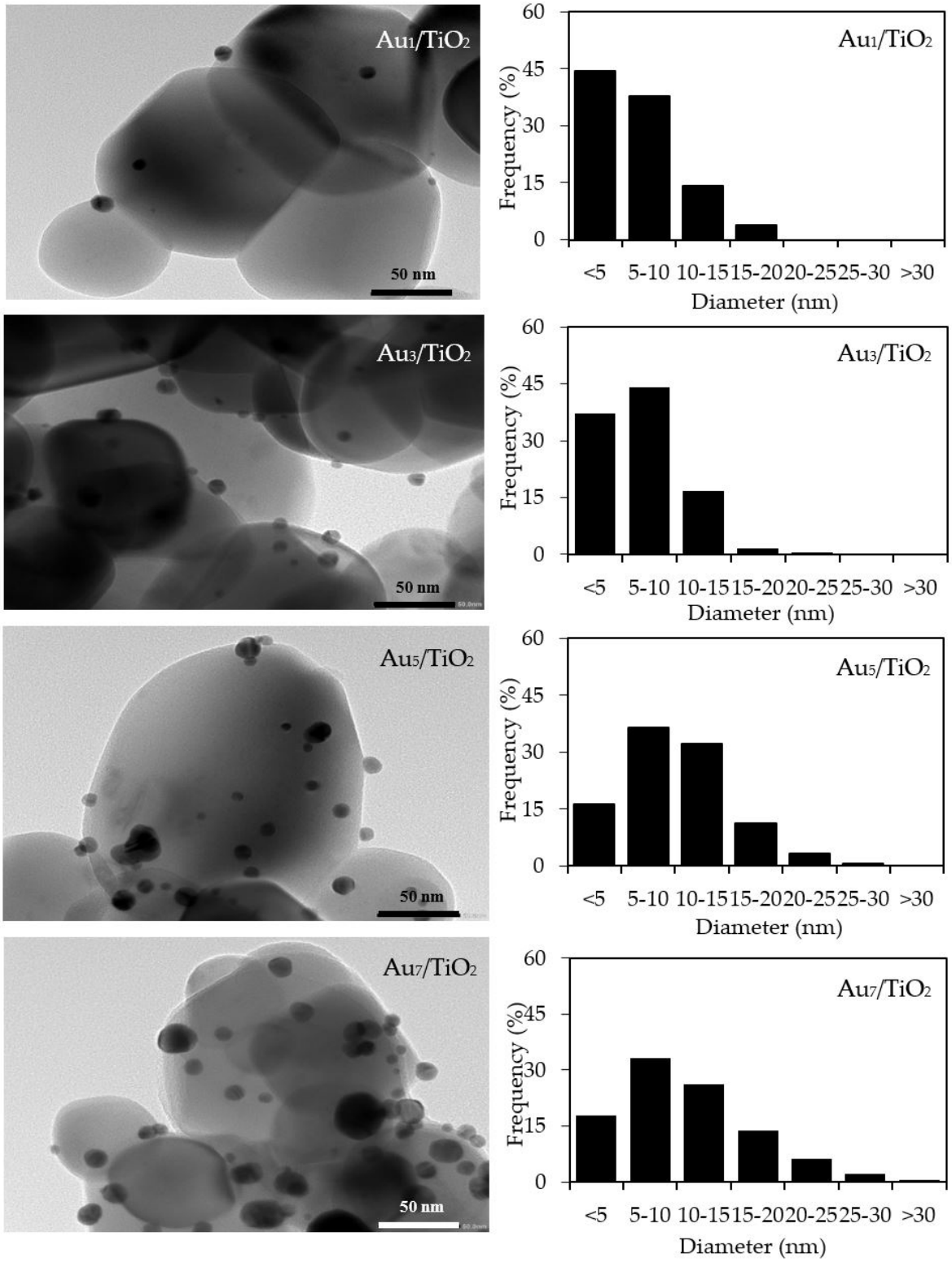

Figure 3. (**Left**) Representative TEM images of the different Au_x/TiO_2 photocatalysts, and (**Right**) the derived Au nanoparticle (NP) size distribution on the surface of the TiO_2.

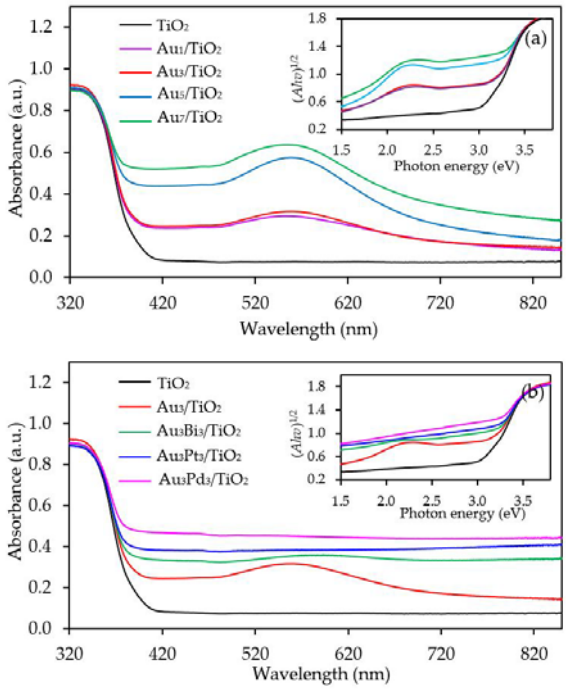

Figure 4. Representative ultra violet-visible (UV-Vis) spectra of the TiO_2 and different (**a**) Au_x/TiO_2 and (**b**) Au_3M_3/TiO_2 photocatalysts with (insert) the respective Tauc's plots.

To confirm the formation of defective structure of TiO_2 in the presence of Au NPs, XPS analysis with a high resolution (HR) Ti2p state was employed. As demonstrated in Figure 5a, two symmetrical peaks at 459.4 and 465.1 eV, assigned to $Ti2p_{3/2}$ and $Ti2p_{1/2}$, were exhibited in the Ti2p core-level spectra of all the prepared Au_x/TiO_2 photocatalysts. The different binding energy of the observed spin-orbit splitting between the $Ti2p_{3/2}$ and $Ti2p_{1/2}$ was around 5.7 eV, in accordance with the typical value of Ti^{4+} sites coordinated to oxygen atoms in TiO_2 [61]. Interestingly, two additional tailored peaks were observed at a lower binding energy of around 457.9 and 464.0 eV, which can be ascribed to the existence of Ti^{3+} species. The generation of Ti^{3+} could have originated from the incorporation of the decorated-metal on the TiO_2 under the H_2 treatment [62,63]. This is because the decorated metal, Au in this case, can induce the generation of oxygen vacancies that are subsequently essential to form the Ti^{3+}-O^{-}-Ti^{4+} defect structures [64]. After deconvolution, the relative content of Ti^{3+}/Ti^{4+} in all the Au_x/TiO_2 photocatalysts was obtained, and is summarized in Table 1. The Ti^{3+}/Ti^{4+} ratio increased as the Au content increased, becoming almost two-fold higher in Au_7/TiO_2 than in Au_1/TiO_2, suggesting that the decoration of TiO_2 with a high Au content induced a high content of Ti^{3+} defective structures in the TiO_2.

With respect to the valence state of the decorated metal, the Au 4f level spectra were also examined. All the prepared photocatalysts displayed the main Au $4f_{7/2}$ and Au $4f_{5/2}$ peaks at a binding energy of about 84.0 and 87.7 eV with a spin-orbit splitting of 3.7 eV (Figure 5b), which are in excellent agreement with the values of the monometallic Au^0 state [65]. Therefore, the Au NPs existed totally in metallic form on the surface of the as-prepared Au_x/TiO_2 photocatalysts. No shift in the Au 4f binding energy was observed, suggesting that the addition of Au within the investigated weight content (1–7 wt. %) did not alter the chemical state of the decorated Au NPs on the TiO_2.

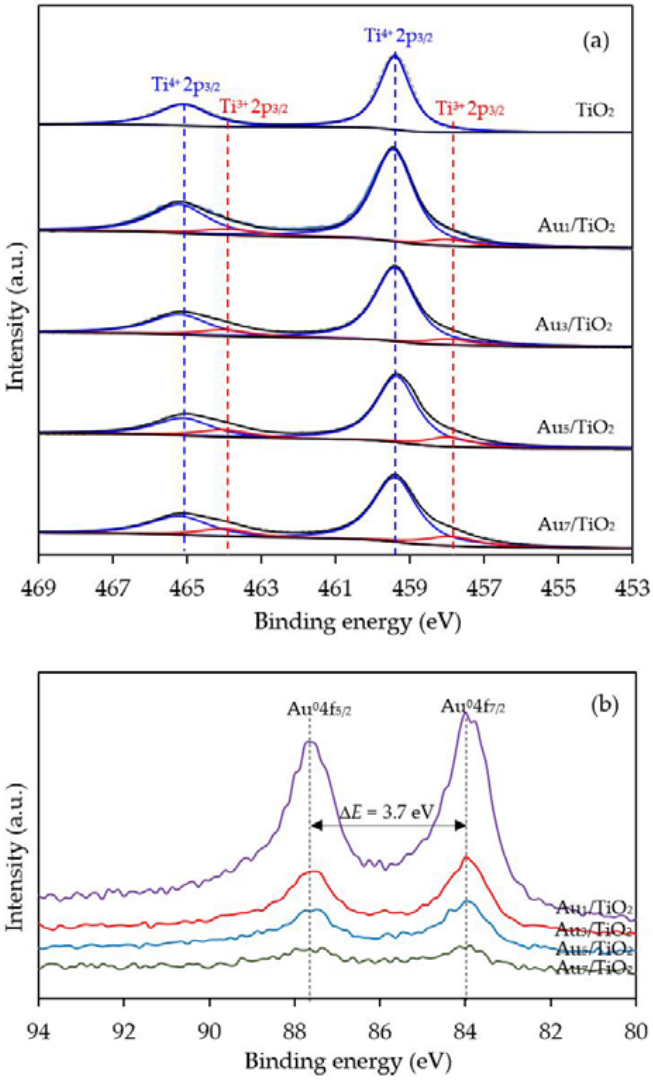

Figure 5. Representative c spectra of the (**a**) Ti2p and (**b**) Au4f of the TiO_2 and different Au_x/TiO_2 photocatalysts.

3.1.2. Photocatalytic Activity

The glycerol conversion in the presence of the different Au_x/TiO_2 photocatalysts is summarized in Figure 6a. All the Au_x/TiO_2 photocatalysts significantly enhanced the glycerol conversion compared to the bare TiO_2. The glycerol conversion increased as the Au content increased from 1 wt. % to 7 wt. %. Plotting the data with the pseudo first order reaction kinetic model (Figure 6b), where a plot of ln (C_t/C_0) versus t provides a straight line and allows the determination of the kinetic rate constant (k), gave a good fit with a determination coefficient (R^2) of greater than 0.9879. Accordingly, the kinetic rate constant of glycerol conversion over the Au_1/TiO_2, Au_3/TiO_2, Au_5/TiO_2 and Au_7/TiO_2 photocatalysts were deduced to be 0.0340, 0.0480, 0.0537 and 0.0606 h^{-1}, respectively, compared to 0.021 h^{-1} for TiO_2 (inset of Figure 6b). The enhanced glycerol conversion over Au-decorated TiO_2 could have arisen from the plasmon induction effect of Au NPs. In addition, the presence of Au NPs was able to serve as electron sinks to facilitate interfacial electron transfer, which could effectively reduce the recombination rate of photogenerated holes (h^+) and electrons (e^-) [66].

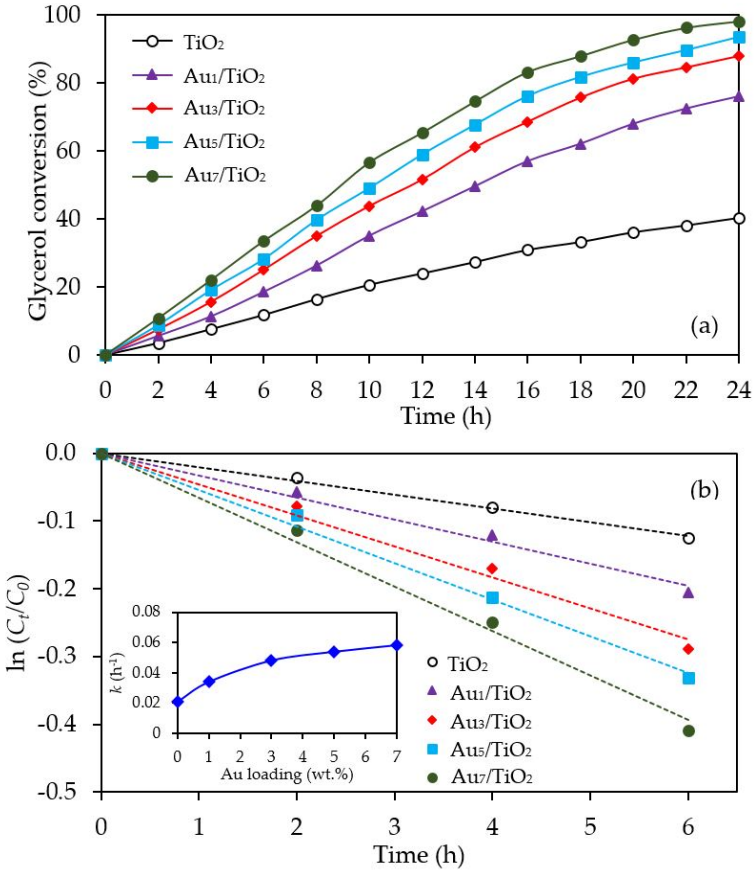

Figure 6. Representative (**a**) glycerol conversion and (**b**) plot of ln (C_t/C_0) as a function of time in the presence of the TiO_2 or different Au_x/TiO_2 (x = 1–7) photocatalysts at a loading of 3.0 g/L, light intensity of 4.7 mW/cm^2 and using O_2 as the electron acceptor.

With respect to the chemical species generated from the glycerol conversion via the photocatalytic oxidation process in the presence of the Au_x/TiO_2 photocatalysts, similar chemical species, including GCD, DHA, HPA, GCOA, FMD and GCAD, were generated via photocatalytic oxidation with the Au_x/TiO_2 photocatalysts as well as with the parent TiO_2 (Figure 7), where GCD was the main product. However, the GCD yield as a function of reaction time varied with the different Au NP contents on the Au_x/TiO_2 photocatalysts. The yield of GCD increased continuously in the presence of 1 wt. % Au_1/TiO_2 from the initial time to the end of reaction time, but in the presence of a high Au content (Au $\geq$ 3 wt. %), the yield of GCD increased continuously to reach a maximum value of around 22% and then dropped slightly. The Au_x/TiO_2 photocatalysts with a high Au NP content enhanced the fast generation of GCD to a maximum level and then accelerated the conversion of GCD to other chemical species, as seen by the decreased GCD yield in the later reaction times. This suggested that the Au_x/TiO_2 photocatalysts with a higher Au content had a higher photocatalytic activity than those with a lower Au content. This was presumably due to their higher content of defective structures, which could promote the visible light absorption due to the narrowing of the electronic bandgap via the continuum interstate between the Ti3d states of the conduction band and the O2p states of the valence band [67]. A high quantity of absorbed photons can achieve a high level of photogenerated h^+ and e^- on the TiO_2 surface. Moreover, the function of the decorated Au NPs as an electron sink can also promote the lifetime of the photogenerated h^+ and e^-, and so enhanced the photocatalytic activity for glycerol conversion.

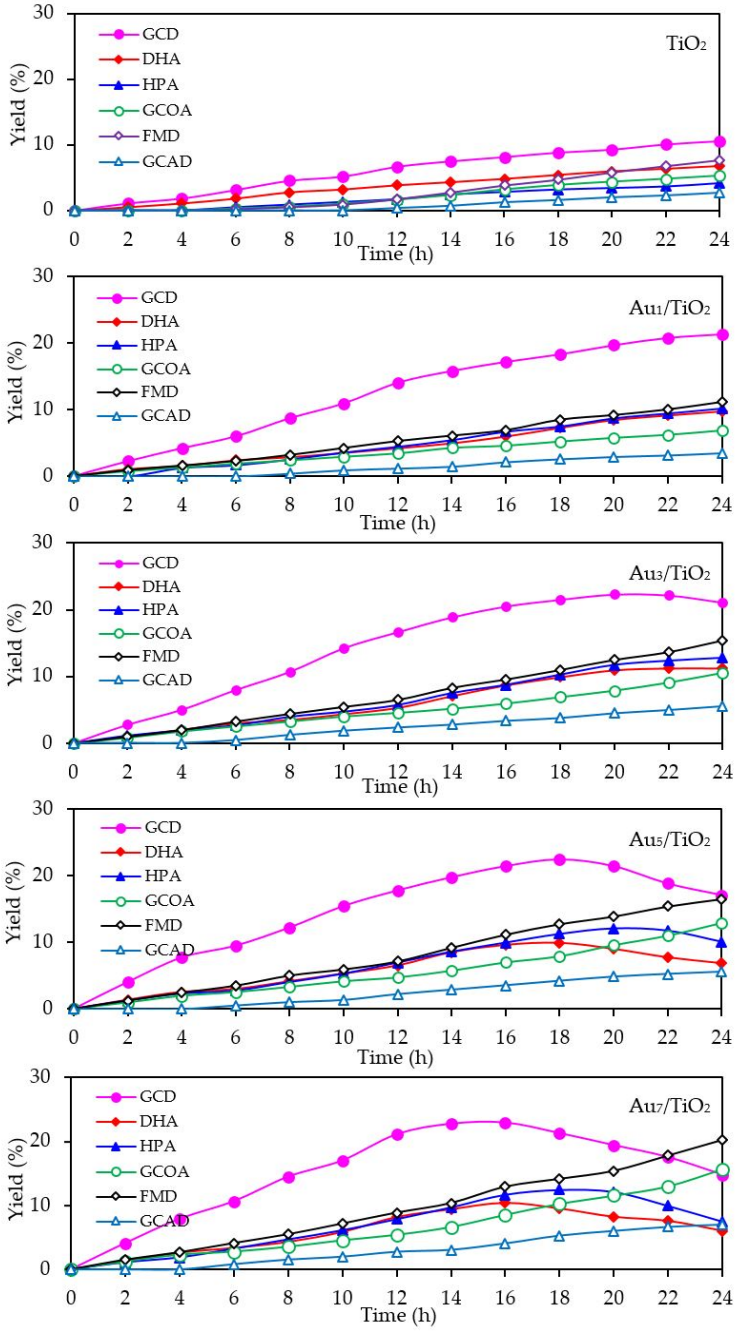

Figure 7. Yield of selected products obtained from the glycerol photocatalytic conversion via the TiO_2 and different Au_x/TiO_2 photocatalysts at a loading of 3.0 g/L, light intensity of 4.7 mW/cm^2 and using O_2 as the electron acceptor.

The mechanism of glycerol conversion to GCD, DHA, HPA, GCOA, FMD and GCAD has been proposed previously [12,68,69]. In brief, the photocatalytic oxidation of glycerol via TiO_2 occurred mainly at the 1°-OH groups to form GCD as the principle product and partially occurred at the 2°-OH group to form DHA. The generated GCD can then be further oxidized with hydroxyl radicals ($HO^{\bullet}$) to form GCOA and FMD, while the DHA is then further oxidized with oxygen species ($O_2^{\bullet-}/{}^1O_2$) to form HPA. The generation of a low GCAD content was probably caused by the adsorption of two molecules of generated FMD on two neighboring Ti^{3+} defective sites and their subsequent dimerization to form GCAD.

3.2. Au_3M_3/TiO_2 Photocatalysts

According to the results obtained, to further explore the role of decorated bimetallic NPs and enhance the glycerol conversion efficiency and yield of product distribution, the Au_3/TiO_2 photocatalyst was selected to composite with other three metals (Bi, Pt and Pd) at the same loading of 3 wt. %.

3.2.1. Photocatalyst Morphology

The XRD patterns of the prepared Au_3M_3/TiO_2 photocatalysts are displayed in Figure 1b. All three exhibited the main diffraction peaks of TiO_2 in the anatase phases, while the diffraction peak of Au NPs was still clearly observed in the XRD patterns of the Au_3/TiO_2 and Au_3Bi_3/TiO_2 photocatalysts, but was not observed in the Au_3Pt_3/TiO_2 and Au_3Pd_3/TiO_2 photocatalysts (Figure 1b_1). A clear diffraction peak of Bi in the rhombohedral lattice appeared separately at a 2θ of 27.0° (PDF No. 01-085-1329) (Figure 1b_1), while no separate peak of Pt and Pd was clearly observed, probably due to their alloy formation with Au NPs. The track of AuPt and AuPd peaks was detected, as shown in Figure 1b_2,b_3. The presence of Au and the respective M in all three Au_3M_3/TiO_2 photocatalysts was close to the set values (3 wt. % of both Au and M), as confirmed by the SEM–EDS analysis (Figure 8), and are listed in Table 1.

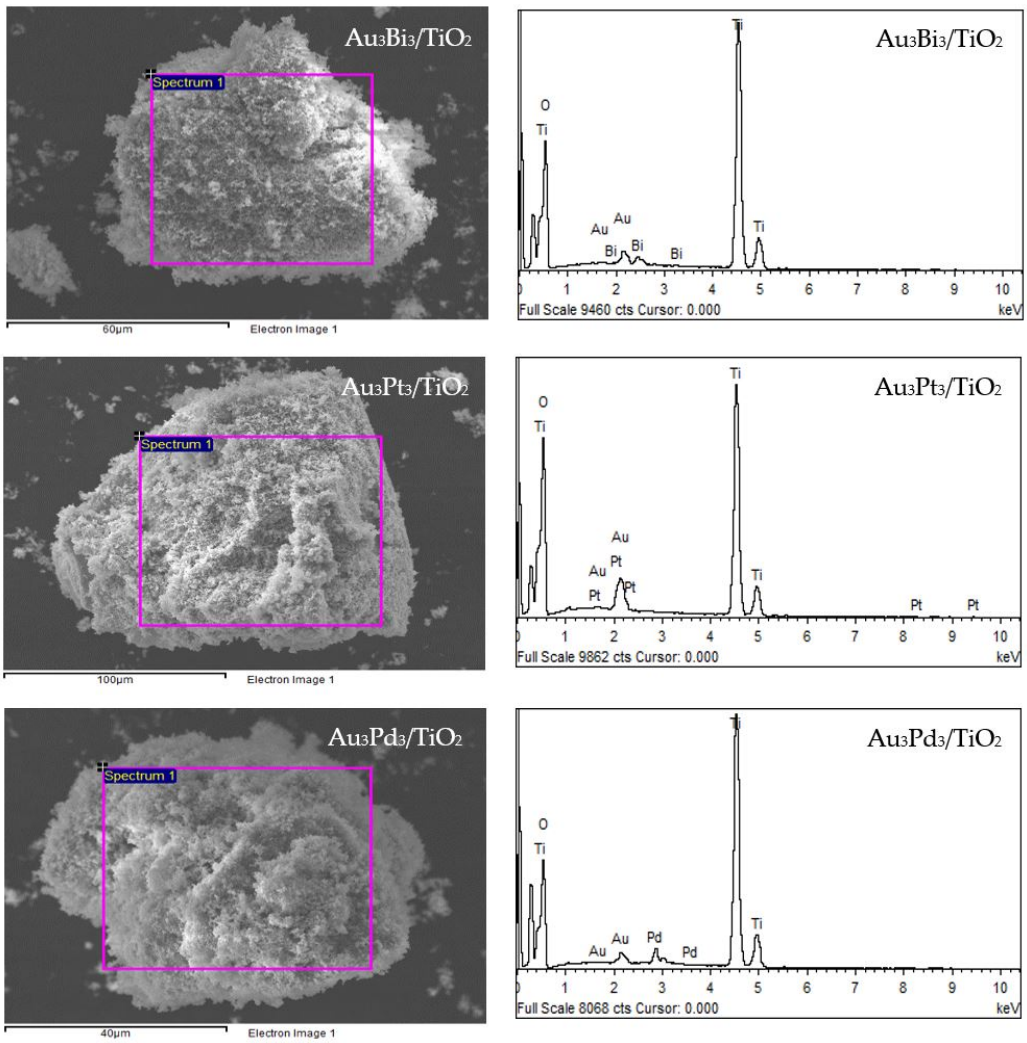

Figure 8. (**Left**) Representative SEM images of the different Au_3M_3/TiO_2 photocatalysts and (**Right**) EDS elemental analysis of the corresponding area shown in the rectangle on the SEM image.

With respect to the particle size distribution, the TEM images (Figure 9) revealed a well-dispersed and narrow size distribution of the decorated AuM NPs on the TiO_2 surface, with a slightly larger particle size than that in Au_3/TiO_2 (Table 1). This suggests that the addition of the second metal induced a slight agglomeration of the AuM NPs. To get insight into the morphology of the decorated metal NPs in the bimetallic catalysts, EDS line-scanning together with the elemental mapping analysis was performed. The compositional line scan of the Au_3Bi_3/TiO_2 photocatalyst showed that the concentration of Au increased from the edge to the center of the metal particle, whereas the Bi distribution was almost constant from the edge to the center of the selected particle (Figure 10a), indicating a core–shell structure of the Bi–Au particle with Au as the core and Bi as the shell. The onset position of the Bi signal was around 0.13 μm, which was 0.008 μm lower than that of Au, indicating a 8 nm thickness of the dendritic Bi shell. A core–shell structure was also observed for the Au_3Pd_3/TiO_2 photocatalyst, in which the high density of Au appeared at the center of the metal particle, while Pd was distributed uniformly from the edge to the center (Figure 10c), with the thickness of the dendritic Pd shell around the Au core being 7.5 nm. A different pattern of the line scan profile was observed for the Au_3Pt_3/TiO_2 photocatalyst, in which the density of both Au and Pt NPs increased from the edge to the center of the selected particle (Figure 10b). This indicated that the AuPt ensembles existed as a solid solution of arbitrary composition or as an AuPt alloy form.

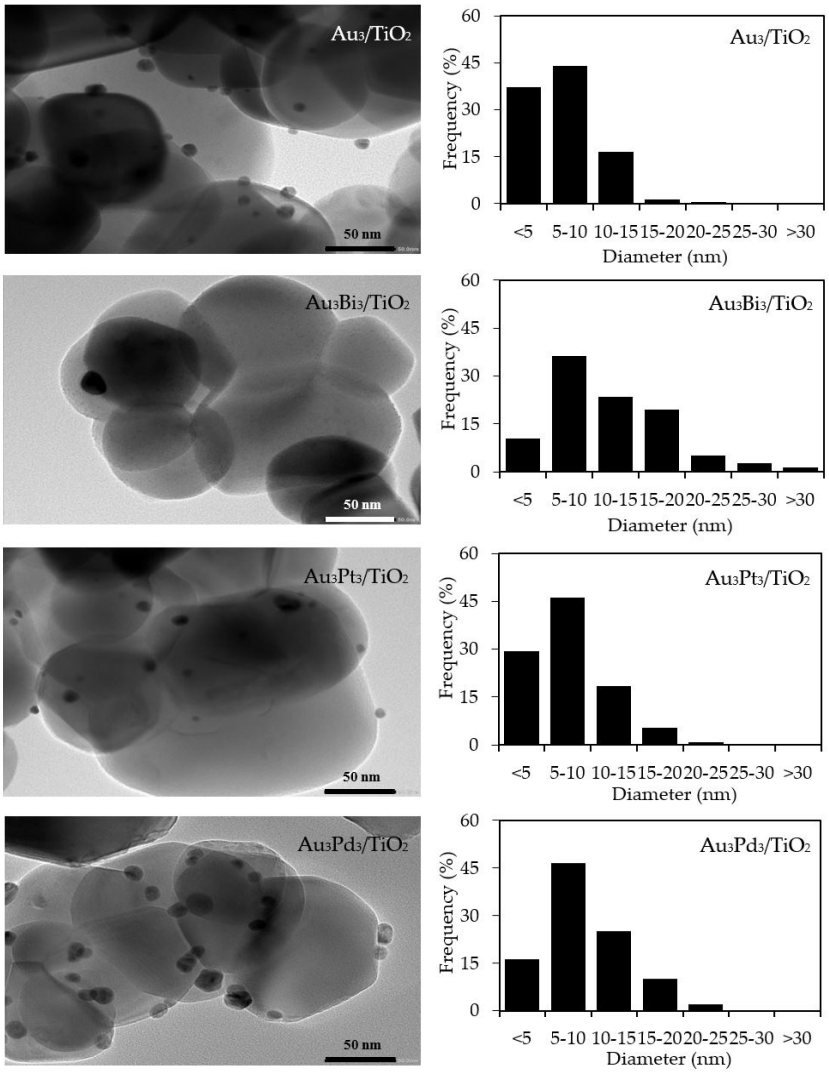

Figure 9. (**Left**) Representative TEM images of the Au_3/TiO_2 and different Au_3M_3/TiO_2 photocatalysts and (**Right**) the derived respective AuM NP size distribution on the surface of the TiO_2.

The capability of UV-vis absorption spectra of the Au_3M_3/TiO_2 photocatalysts is shown in Figure 4b, where they all exhibited a high capability to absorb visible light at a wavelength of greater than 400 nm. The addition of Bi, Pt or Pd to the Au_3/TiO_2 attenuated an intense broad absorption band centered at around 540 nm of Au, probably due to the different dielectric function of the bimetals compared to the Au monometallic state [70]. Moreover, the strong interaction between the decorated Au–M can also influence the flattening of the Au LSPR band [71]. The bandgap values of the Au_3Bi_3/TiO_2, Au_3Pt_3/TiO_2 and Au_3Pd_3/TiO_2 photocatalysts, as determined from a Tauc's plot (inset of Figure 4b), were 2.85, 2.85 and 2.79 eV, respectively (Table 1), which suggested that the addition of the respective second metal caused the generation of the defective structure of TiO_2. The formation of the Ti^{3+} defect structure likely induced an altered major electronic state of the valence band and conduction band, by which it formed a mid-gap state below the conduction band and also enabled the lengthening of the conduction band edge, resulting in the formation of the band tail structure and the narrowness of the bandgap energy [72].

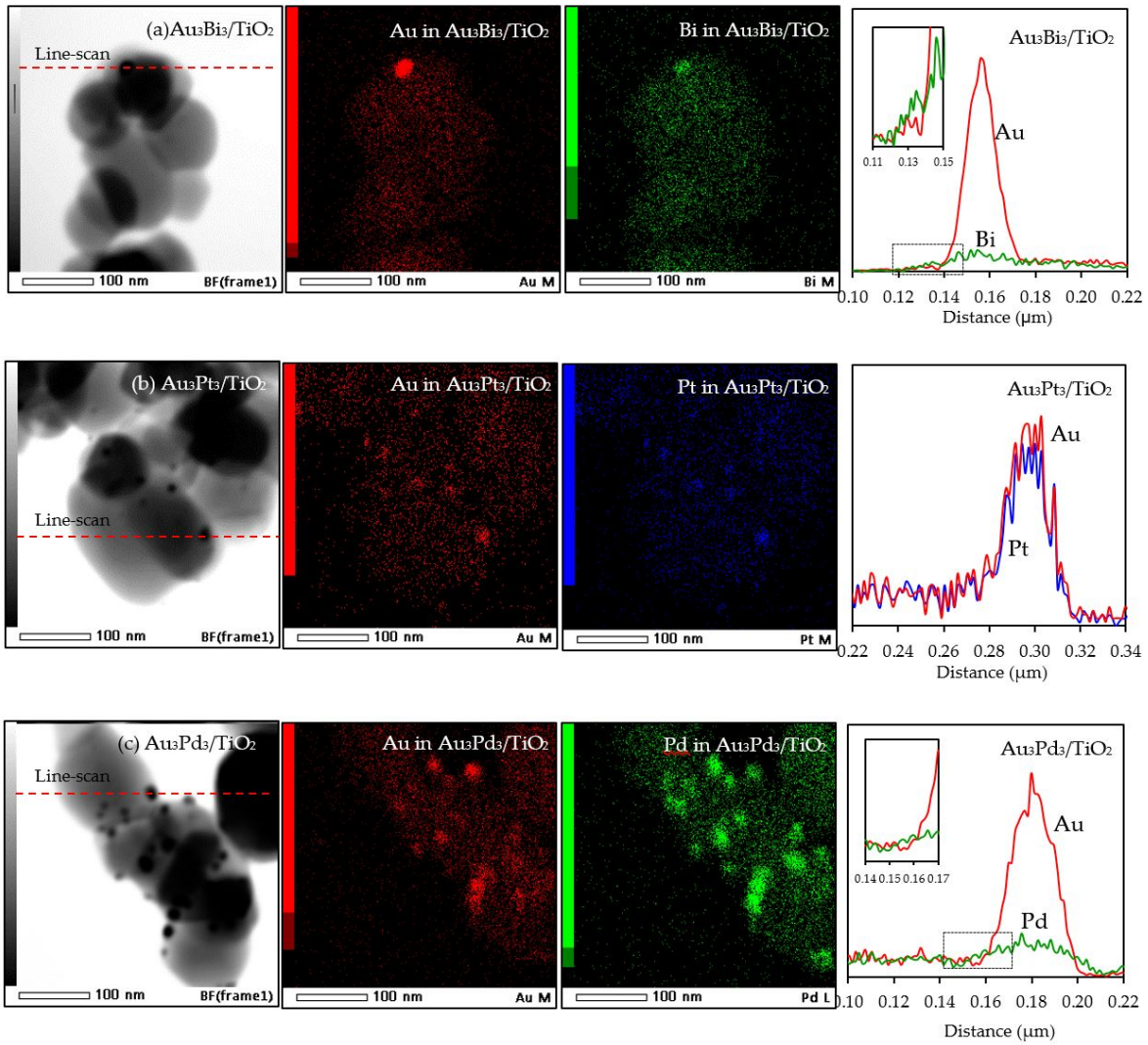

Figure 10. Representative TEM–EDS mapping images and line-scan profile of the different of Au_3M_3/TiO_2 photocatalysts.

To confirm the presence of the Ti^{3+} defective structures, Ti2p HR-XPS spectra of the Au_3M_3/TiO_2 photocatalysts were investigated, and are shown in Figure 11a. The core-level Ti2p spectra still exhibited the two main symmetric peaks of Ti $2p_{3/2}$ and Ti $2p_{1/2}$ at a binding energy of 459.4 and

465.1 eV, respectively, with a difference of 5.7 eV, in accordance with the typical value of the Ti^{4+} state in TiO_2. The shoulder peak of Ti2p at a low binding energy, assigned to the existence of the Ti^{3+} structure, was distinctly observed in all the Au_3M_3/TiO_2 photocatalysts. The Ti^{3+}/Ti^{4+} ratios, as obtained from the area under the deconvolution of both peaks, are listed in Table 1. The Au_3M_3/TiO_2 photocatalysts all exhibited a higher Ti^{3+}/Ti^{4+} ratio than the Au_3/TiO_2 and parent TiO_2 photocatalysts, indicating that the addition of the bimetallic NPs (Au–Bi, Au–Pt and Au–Pd) induced a greater content of defective structures of TiO_2 than the addition of the monometallic Au NPs. Among all the Au_3M_3/TiO_2 photocatalysts, surprisingly, the Au_3Pd_3/TiO_2 photocatalyst exhibited the highest Ti^{3+}/Ti^{4+} ratio of 0.3561, which was 2.41-, 1.82- and 1.83-fold higher than that of the Au_3/TiO_2, Au_3Bi_3/TiO_2 and Au_3Pt_3/TiO_2 photocatalysts, respectively. The higher content of Ti^{3+} defect species in the bi- than mono-metallic system might be because the high content of decorated metal can incorporate into the TiO_2 structure and induce formation of the Ti^{3+} defect site by transferring electrons between the decorated metal and oxygen vacancies of TiO_2 in order to maintain the charge balance [73].

To distinguish the valence states of the decorated metal, the Au 4f level spectra of all Au_3M_3/TiO_2 photocatalysts were analyzed, with respective examples shown in Figure 11b. The two main characteristic peaks of Au $4f_{7/2}$ and Au $4f_{5/2}$ were still observed with a spin-orbit splitting of 3.7 eV, indicating the presence of Au in the metallic state. A slight blue shift in the Au 4f binding energy was observed for the Au_3Pt_3/TiO_2 and Au_3Pd_3/TiO_2 photocatalysts in comparison with that of Au_3/TiO_2. Typically, the shift in the binding energy in each metal is attributed to various factors, such as a change in its chemical state or the charge compensation of added elements on the parent elements. However, in this case, the chemical state of Au in all the Au_3M_3/TiO_2 photocatalysts was still in the metallic state (Figure 11b), and so this blue shift in the Au binding energy could be the result of charge compensation of the Pt or Pd elements on Au elements [74], by which Au accepted *sp*-electrons from Pt or Pd, but donated *d*-electrons to Pt or Pd, and possibly due to the partial formation of Au–M alloy structure, which are more negatively charged [75]. A low Au 4f intensity was observed in the case of the Au_3Bi_3/TiO_2 photocatalyst compared with other two Au_3M_3/TiO_2 photocatalysts, due to the presence of the Bi-wrapped Au NPs as a core–shell structure.

The chemical state of the second metal in all the photocatalysts was also analyzed by the HR-XPS. As demonstrated in Figure 12, all the second metals in the respective Au_3M_3/TiO_2 photocatalysts were presented in both metallic and oxide forms. The peaks located at 162.9 eV and 157.6 eV for the Au_3Bi_3/TiO_2 photocatalyst were assigned to Bi^0 $4f_{5/2}$ and Bi^0 $4f_{7/2}$, respectively, which is the characteristic value of the metallic Bi. A further two peaks at 164.5 eV and 159.2 eV were assigned to the $Bi^{3+}4f_{5/2}$ and $Bi^{3+}4f_{7/2}$ region, which are characteristic of Bi^{3+} in the as-prepared catalysts. These binding energy values of the Bi^{3+} ion-valent-form are too high to be assigned to the typical Bi^{3+} in bismuth oxide (Bi_2O_3), but rather were assigned to bismuth hydroxylated oxide (BiO(OH)) species on the photocatalyst surface [76]. For the Au_3Pt_3/TiO_2 photocatalyst, the Pt 4f signals consisted of three pairs of doublets; the Pt^0 $4f_{5/2}$ and Pt^0 $4f_{7/2}$ peaks at binding energies of 74.2 eV and 70.9 eV, the Pt^{2+} $4f_{5/2}$ and Pt^{2+} $4f_{7/2}$ peaks at binding energies of 75.3 eV and 72.0 eV and the Pt^{4+} $4f_{5/2}$ and Pt^{4+} $4f_{7/2}$ peaks at binding energies of 76.5 eV and 73.2 eV, with an identical spin-orbit splitting of about 3.3 eV [77]. This suggests that the Pt NPs were present in both metallic zero-valent (Pt^0) and metallic ion-valent (Pt^{2+} and Pt^{4+}) forms. For the Au_3Pd_3/TiO_2 photocatalyst, the most intensive doublet, at binding energies of 340.6 eV (Pd^0 $3d_{3/2}$) and 335.3 eV (Pd^0 $3d_{5/2}$), was attributed to metallic Pd. The shoulder peaks located at binding energies of around 342.2 eV and 336.9 eV were assigned to Pd^{2+} $3d_{3/2}$ and Pd^{2+} $3d_{5/2}$, respectively, which is characteristic of Pd^{2+} in PdO in the achieved catalyst. The spin-orbit splitting of about 5.3 eV in both the metallic Pd and Pd^{2+} was well in accordance with the reported value [14]. All the second metal NPs in the respective Au_3M_3/TiO_2 catalysts existed predominantly in the metallic form, whereas the partial presence of the second metal in an oxide form might be attributed to the formation of a M–O bond driven by the oxygen chemisorption on the surface of the second metal nanostructure during the prepa ration process.

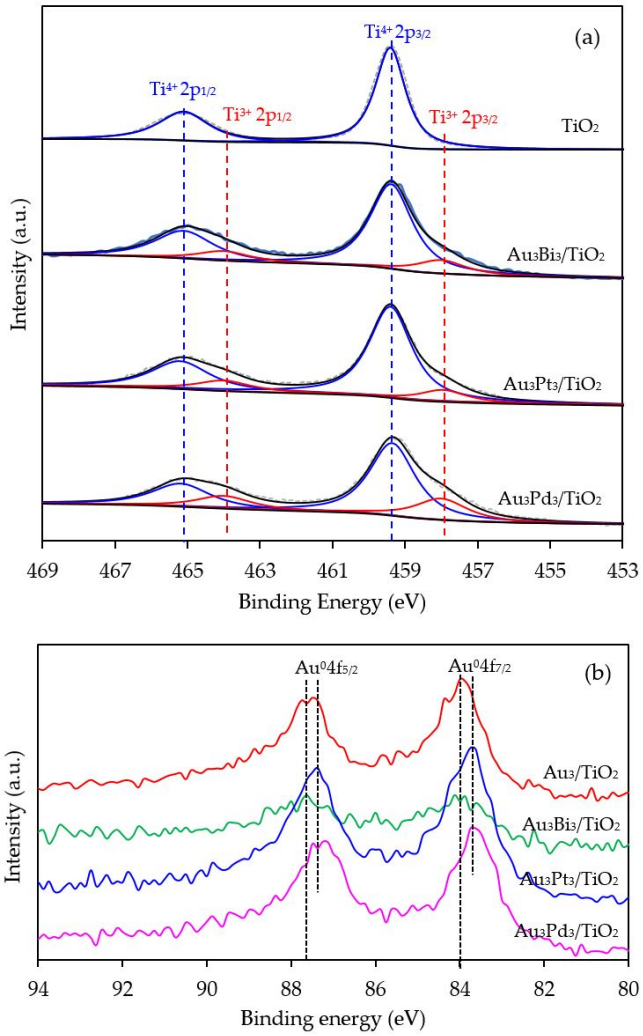

Figure 11. Representative HR-XPS spectra of (**a**) Ti2p and (**b**) Au4f of the TiO_2, Au_3/TiO_2 and the different Au_3M_3/TiO_2 photocatalysts.

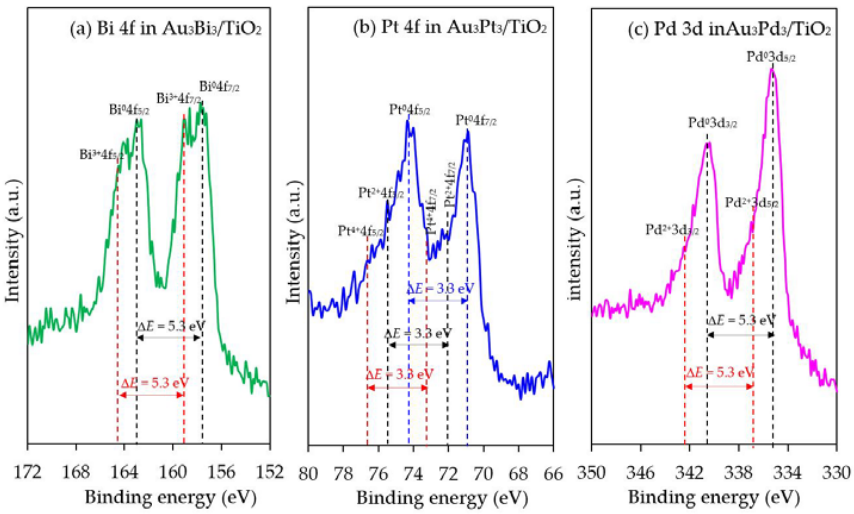

Figure 12. Representative HR-XPS spectra of Bi 4f, Pt 4f and Pd 3d in the respective Au_3M_3/TiO_2 photocatalysts.

3.2.2. Photocatalytic Activity

The photocatalytic activity of the Au_3M_3/TiO_2 photocatalysts was tested for the photocatalytic oxidation of glycerol to selected value-added compounds. As demonstrated in Figure 13a, the addition of Pt or Pd NPs on the Au_3/TiO_2 photocatalyst to form Au_3Pt_3/TiO_2 and Au_3Pd_3/TiO_2, respectively, enhanced the glycerol conversion, while the addition of Bi NPs retarded the reaction. The first order kinetic rate constants of glycerol conversion over Au_3Bi_3/TiO_2, Au_3Pt_3/TiO_2 and Au_3Pd_3/TiO_2 were 0.0396, 0.0644 and 0.0810 h^{-1}, respectively (Figure 13b). The Au_3Bi_3/TiO_2 photocatalyst exhibited a lower photocatalytic activity than the Au_3/TiO_2 photocatalyst despite having a lower bandgap energy and higher defective structure, probably due to the core–shell structure of the AuBi NPs. That is, the LSPR behavior of the Au NPs was diminished when they were wrapped by the Bi species. Moreover, the decorated Bi NPs cannot extract the excited e^- from the Au or supported TiO_2 due to its lower work function (4.22 eV) than that of Au (5.1 eV) and TiO_2 (4.9 eV), resulting in unalleviated e^--h^+ recombination (Figure 14a). The high photocatalytic activity of the Au_3Bi_3/TiO_2 compared to the parent TiO_2 was due to the presence of the valence band tail above the valence band, which was caused by the hybridization of the Bi 6s and O 2p orbital, and the existence of the Ti^{3+} state below the conduction band [53], which allowed an easy jump of photogenerated e^- from either the valence band tail level to either a shallow trap (Ti^{3+} state) or conduction band. In addition, as previously mentioned, the Bi6s is widely dispersed in the hybrid orbital of Bi6s-O2p leading to an increased charge mobility and consequently an improved photocatalytic activity of the parent photocatalyst [78].

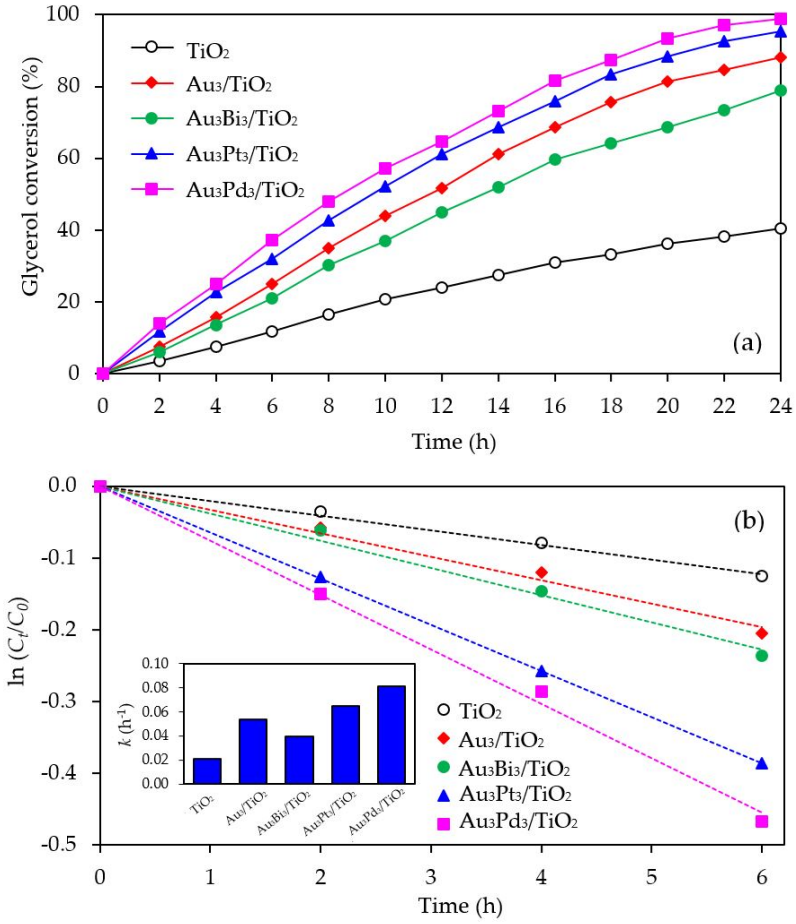

Figure 13. Representative (**a**) glycerol conversion and (**b**) a plot of ln (C_t/C_0) as a function of time in the presence of the respective Au_3M_3/TiO_2 photocatalyst at a loading of 3.0 g/L, light intensity of 4.7 mW/cm^2 and using O_2 as the electron acceptor.

For the Au_3Pt_3/TiO_2 and Au_3Pd_3/TiO_2 photocatalysts, the enhanced glycerol conversion compared with the Au_3/TiO_2 photocatalyst was probably due to their lower bandgap energy, which allowed the electron excitation at a lower photon energy and the presence of LSPR behavior in the decorated noble metal structure, resulting in the transfer of e^- from the metallic NPs to a shallow trap or conduction band of TiO_2, or vice versa, under the light absorption. Moreover, in fact, the excited electron can be transferred by the driven work function. The difference in work function between Au and the second metal (Pt or Pd) can reduce the e^--h^+ recombination rate by transferring the e^- between the two metals after trapping the e^- from the conduction band of TiO_2 into equilibrium [79]. That is, the work function of Au is 5.1 eV and those of Pt and Pd are 5.65 eV and 5.22 eV, respectively. The decorated Au–Pt NPs formed an alloy structure in the Au_3Pt_3/TiO_2 photocatalyst, which can initiate a new Fermi level of alloy NPs somewhere between the Fermi level of Au and Pt (Figure 14b) and so could prolong the e^--h^+ lifetime compared with the Au–Bi NPs. This was shorter than the two-stage transferring of an excited electron between the two individual Fermi levels of each decorated metal in the core–shell structure generated in the Au_3Pd_3/TiO_2 photocatalyst (Figure 14c). This is the reason why the Au_3Pd_3/TiO_2 exhibited a higher photocatalytic activity than the Au_3Pt_3/TiO_2 photocatalyst.

The core–shell structure of the Au_3Pd_3/TiO_2 photocatalyst did not exhibit a negative effect on the LSPR behavior in this photocatalyst, probably because the plasmon metallic state of Pd can still occur, leading to an easy transfer of e^- from the TiO_2 conduction band to Pd NPs and/or Au NPs and vice versa.

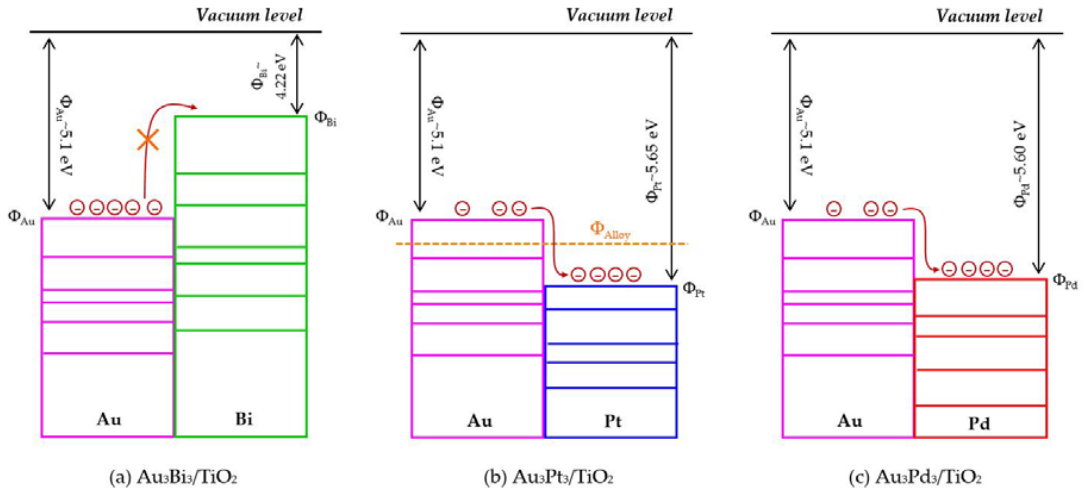

Figure 14. Schematic profiles of the contact metal with work function in the bimetallic NPs system.

With respect to the generated products, the same products (GCD, DHA, HPA, GCOA, FMD and GCAD) were generated via all the Au_3M_3/TiO_2 photocatalysts and were similar to those generated in the presence of either the Au_3/TiO_2 or parent TiO_2 photocatalyst (Figure 15). The principle product was GCD in the presence of all the evaluated photocatalysts except for Au_3Bi_3/TiO_2, where GCAD was the principle product. As reported previously [53], monometallic Bi NPs decorated on TiO_2 did not promote the formation of GCAD as a major product. Accordingly, it is suggested that the synergism between the bimetallic Au–Bi was a vital factor in the formation of GCAD from glycerol. Various published works on the aerobic oxidation of glycerol over bimetallic catalysts with Bi NPs have proposed that Bi played a major role as a geometric blocking site, which can facilitate the activation and transformation of the secondary hydroxyl group of glycerol [54–56]. In this present work, glycerol was mainly converted through the photocatalytic oxidation reaction over Au_3Bi_3/TiO_2 to GCAD as the major product. It is hypothesized that the two terminal hydroxyl (-OH) groups of glycerol were bound on the surface of the Au–Bi NPs with Bi^{3+} species, whereas Bi adatoms function as blockers on the Au site, which is a high-energy site where the adsorption and reaction of the primary –OH group

is preferred. This then serves to control the adsorbed orientation of glycerol molecules towards the preferential oxidation of the secondary –OH group to form DHA. In addition, due to the presence of various reactive oxygen species with a high oxidizing power in the photocatalytic system, the cleavage of the C–C bond of the generated DHA molecule to one molecule of GCAD and FMD is dramatically achieved. The generated FMD can eventually be oxidized to form CO_2 as a gas-phase oxidation product. However, the synergetic role of Bi and the optimization of the Bi-promoted Au or other noble metals on TiO_2 photocatalyst with the corresponding reaction conditions act to determine the highly selective oxidation of glycerol, which could also work to some extent that might be beneficial in academic research and the chemical industry.

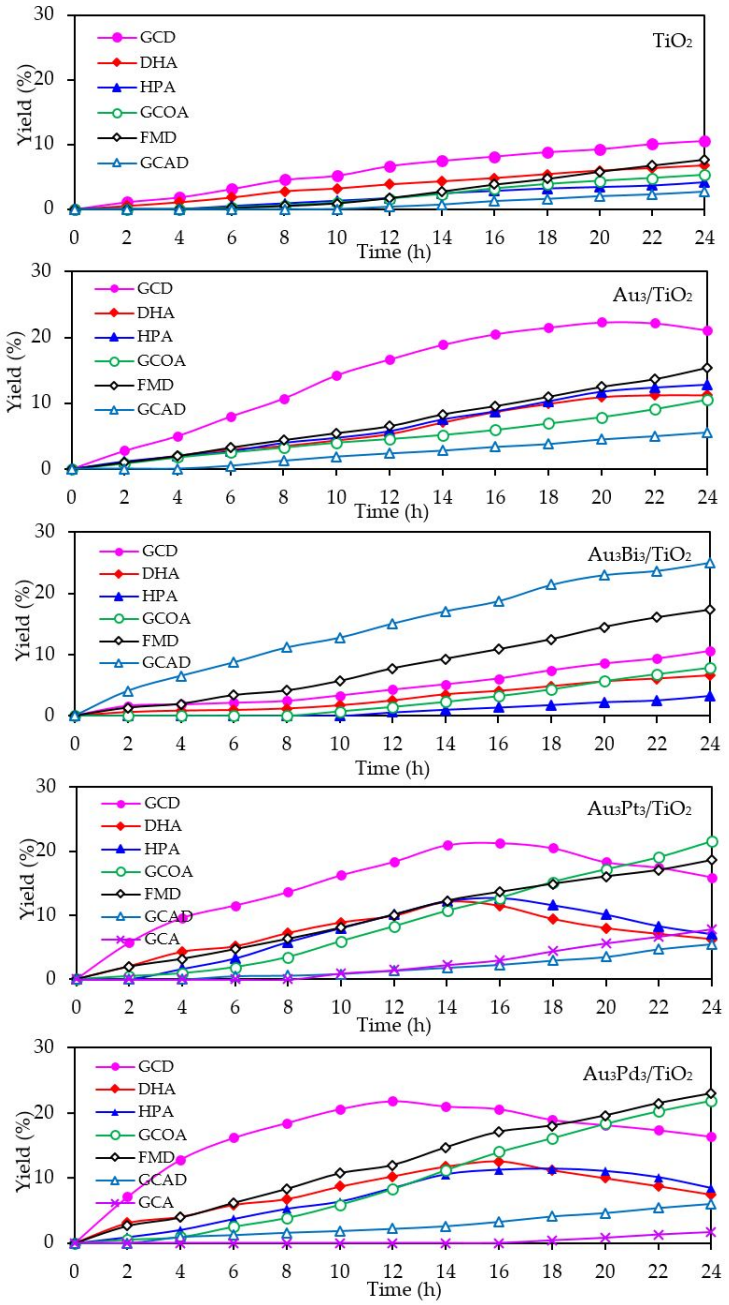

Figure 15. Yield of selected products obtained from the glycerol photocatalytic conversion via the TiO_2, Au_3/TiO_2 and respective Au_3M_3/TiO_2 photocatalysts at a loading of 3.0 g/L, light intensity of 4.7 mW/cm^2, and using O_2 as the electron acceptor.

4. Conclusions

Monometallic Au NPs with different metal contents and three types of Au-based bimetallic NPs (Au–Bi, Au–Pt and Au–Pd) with a nominal metal content of 3 wt. % were decorated on TiO_2 by the sol-immobilization technique and then tested for photocatalytic oxidation of glycerol. The decoration of Au NPs in both mono- and bimetallic systems on TiO_2 enhanced the photocatalytic glycerol conversion due to the narrowed bandgap energy and increased light harvesting capability of the as-prepared photocatalysts and the alleviation of e^{-}-h^{+} recombination in the presence of the decorated metal. The Au_3Pd_3/TiO_2 photocatalyst was found to be highly active and the most efficient tested photocatalyst for glycerol conversion, mainly because it had the lowest bandgap energy, the largest Ti^{3+} defect content and highest UV-Visible light absorption ability. The principle liquid phase product in the photocatalytic oxidation of glycerol over the Au_x/TiO_2, Au_3Pt_3/TiO_2 and Au_3Pd_3/TiO_2 photocatalysts was GCD. By contrast, Au_3Bi_3/TiO_2 promoted the generation of GCAD as the major liquid phase product, which might be due to the promotional role of Bi species that act as a chelated site between the glycerol molecules and Au sites. This work paves a new way to undertake the rational design of mono- and bimetallic NPs decorated on TiO_2 in order to enhance the performance of the photocatalytic process and promote the selective photocatalytic oxidation of glycerol.

Acknowledgments: The authors thank the Chulalongkorn University Dutsadi Phiphat Scholarship, the Ratchadapisek Sompoch Endowment Fund, Chulalongkorn University (Sci-Super II GF_58_08_23_01) and the Thailand Research Fund (IRG5780001) for financial support.

Author Contributions: T.J., M.H., and N.S. conceived and designed the experiments; T.J. performed the experiments; T.J., and M.H. analyzed the data; M.H., and N.S. contributed reagents/materials/analysis tools; and T.J., and M.H. wrote the paper.

Conflicts of Interest: The authors declare no conflict of interest.

References

1. Clomburg, J.M.; Gonzalez, R. Anaerobic fermentation of glycerol: A platform for renewable fuels and chemicals. *Trends Biotechnol.* **2013**, *31*, 20–28. [CrossRef] [PubMed]
2. Crotti, C.; Kašpar, J.; Farnetti, E. Dehydrogenation of glycerol to dihydroxyacetone catalyzed by iridium complexes with p–n ligands. *Green Chem.* **2010**, *12*, 1295–1300. [CrossRef]
3. Zou, B.; Ren, S.; Ye, X.P. Glycerol dehydration to acrolein catalyzed by zsm-5 zeolite in supercritical carbon dioxide medium. *ChemSusChem* **2016**, *9*, 3268–3271. [CrossRef] [PubMed]
4. Veiga, P.M.; Gomes, A.C.; Veloso, C.O.; Henriques, C.A. Acid zeolites for glycerol etherification with ethyl alcohol: Catalytic activity and catalyst properties. *Appl. Catal. A Gen.* **2017**, *548*, 2–15. [CrossRef]
5. Hu, W.; Zhang, Y.; Huang, Y.; Wang, J.; Gao, J.; Xu, J. Selective esterification of glycerol with acetic acid to diacetin using antimony pentoxide as reusable catalyst. *J. Energy Chem.* **2015**, *24*, 632–636. [CrossRef]
6. Katryniok, B.; Kimura, H.; Skrzyńska, E.; Girardon, J.-S.; Fongarland, P.; Capron, M.; Ducoulombier, R.; Mimura, N.; Paul, S.; Dumeignil, F. Selective catalytic oxidation of glycerol: Perspectives for high value chemicals. *Green Chem.* **2011**, *13*, 1960–1979. [CrossRef]
7. Villa, A.; Dimitratos, N.; Chan-Thaw, C.E.; Hammond, C.; Prati, L.; Hutchings, G.J. Glycerol oxidation using gold-containing catalysts. *Acc. Chem. Res.* **2015**, *48*, 1403–1412. [CrossRef] [PubMed]
8. Puddu, V.; Choi, H.; Dionysiou, D.D.; Puma, G.L. TiO_2 photocatalyst for indoor air remediation: Influence of crystallinity, crystal phase, and uv radiation intensity on trichloroethylene degradation. *Appl. Catal. B Environ.* **2010**, *94*, 211–218. [CrossRef]
9. Pansa-Ngat, P.; Jedsukontorn, T.; Hunsom, M. Simultaneous H_2 production and pollutant removal from biodiesel wastewater by photocatalytic oxidation with different crystal structure TiO_2 photocatalysts. *J. Taiwan Inst. Chem. Eng.* **2017**, *78*, 386–394. [CrossRef]
10. Low, J.; Cheng, B.; Yu, J. Surface modification and enhanced photocatalytic Co_2 reduction performance of TiO_2: A review. *Appl. Surf. Sci.* **2017**, *392*, 658–686. [CrossRef]
11. Fujita, S.-I.; Kawamori, H.; Honda, D.; Yoshida, H.; Arai, M. Photocatalytic hydrogen production from aqueous glycerol solution using nio/tio2 catalysts: Effects of preparation and reaction conditions. *Appl. Catal. B Environ.* **2016**, *181*, 818–824. [CrossRef]

12. Jedsukontorn, T.; Meeyoo, V.; Saito, N.; Hunsom, M. Route of glycerol conversion and product generation via TiO_2-induced photocatalytic oxidation in the presence of H_2O_2. *Chem. Eng. J.* **2015**, *281*, 252–264. [CrossRef]
13. Zhang, Z.; Wang, Z.; Cao, S.-W.; Xue, C. Au/pt nanoparticle-decorated TiO_2 nanofibers with plasmon-enhanced photocatalytic activities for solar-to-fuel conversion. *J. Phys. Chem. C* **2013**, *117*, 25939–25947. [CrossRef]
14. Bashir, S.; Idriss, H. Mechanistic study of the role of au, pd and au-pd in the surface reactions of ethanol over TiO_2 in the dark and under photo-excitation. *Catal. Sci. Technol.* **2017**, *7*, 5301–5320. [CrossRef]
15. Sellappan, R.; Nielsen, M.G.; González-Posada, F.; Vesborg, P.C.; Chorkendorff, I.; Chakarov, D. Effects of plasmon excitation on photocatalytic activity of ag/TiO_2 and au/TiO_2 nanocomposites. *J. Catal.* **2013**, *307*, 214–221. [CrossRef]
16. Shuang, S.; Lv, R.; Xie, Z.; Zhang, Z. Surface plasmon enhanced photocatalysis of au/pt-decorated TiO_2 nanopillar arrays. *Sci. Rep.* **2016**, *6*, 26670. [CrossRef] [PubMed]
17. Leong, K.H.; Chu, H.Y.; Ibrahim, S.; Saravanan, P. Palladium nanoparticles anchored to anatase TiO_2 for enhanced surface plasmon resonance-stimulated, visible-light-driven photocatalytic activity. *Beilstein J. Nanotechnol.* **2015**, *6*, 428. [CrossRef] [PubMed]
18. Linic, S.; Christopher, P.; Ingram, D.B. Plasmonic-metal nanostructures for efficient conversion of solar to chemical energy. *Nat. Mater.* **2011**, *10*, 911. [CrossRef] [PubMed]
19. Ide, Y.; Matsuoka, M.; Ogawa, M. Efficient visible-light-induced photocatalytic activity on gold-nanoparticle-supported layered titanate. *J. Am. Chem. Soc.* **2010**, *132*, 16762–16764. [CrossRef] [PubMed]
20. Tanaka, A.; Teramura, K.; Hosokawa, S.; Kominami, H.; Tanaka, T. Visible light-induced water splitting in an aqueous suspension of a plasmonic au/TiO_2 photocatalyst with metal co-catalysts. *Chem. Sci.* **2017**, *8*, 2574–2580. [CrossRef] [PubMed]
21. Tanaka, A.; Sakaguchi, S.; Hashimoto, K.; Kominami, H. Photocatalytic reactions under irradiation of visible light over gold nanoparticles supported on titanium (iv) oxide powder prepared by using a multi-step photodeposition method. *Catal. Sci. Technol.* **2014**, *4*, 1931–1938. [CrossRef]
22. Tanaka, A.; Hashimoto, K.; Ohtani, B.; Kominami, H. Non-linear photocatalytic reaction induced by visible-light surface-plasmon resonance absorption of gold nanoparticles loaded on titania particles. *Chem. Commun.* **2013**, *49*, 3419–3421. [CrossRef] [PubMed]
23. Wang, H.; You, T.; Shi, W.; Li, J.; Guo, L. Au/TiO_2/au as a plasmonic coupling photocatalyst. *J. Phys. Chem. C* **2012**, *116*, 6490–6494. [CrossRef]
24. Hvolbæk, B.; Janssens, T.V.; Clausen, B.S.; Falsig, H.; Christensen, C.H.; Nørskov, J.K. Catalytic activity of au nanoparticles. *Nano Today* **2007**, *2*, 14–18. [CrossRef]
25. Brust, M.; Walker, M.; Bethell, D.; Schiffrin, D.J.; Whyman, R. Synthesis of thiol-derivatised gold nanoparticles in a two-phase liquid–liquid system. *J. Chem. Soc. Chem. Commun.* **1994**, 801–802. [CrossRef]
26. Brust, M.; Fink, J.; Bethell, D.; Schiffrin, D.; Kiely, C. Synthesis and reactions of functionalised gold nanoparticles. *J. Chem. Soc. Chem. Commun.* **1995**, 1655–1656. [CrossRef]
27. Haruta, M.; Kobayashi, T.; Sano, H.; Yamada, N. Novel gold catalysts for the oxidation of carbon monoxide at a temperature far below 0 c. *Chem. Lett.* **1987**, *16*, 405–408. [CrossRef]
28. Hutchings, G.J. Vapor phase hydrochlorination of acetylene: Correlation of catalytic activity of supported metal chloride catalysts. *J. Catal.* **1985**, *96*, 292–295. [CrossRef]
29. Wang, J.; Gu, H. Novel metal nanomaterials and their catalytic applications. *Molecules* **2015**, *20*, 17070–17092. [CrossRef] [PubMed]
30. Ayati, A.; Ahmadpour, A.; Bamoharram, F.F.; Tanhaei, B.; Mänttäri, M.; Sillanpää, M. A review on catalytic applications of au/TiO_2 nanoparticles in the removal of water pollutant. *Chemosphere* **2014**, *107*, 163–174. [CrossRef] [PubMed]
31. Fiorenza, R.; Bellardita, M.; D'Urso, L.; Compagnini, G.; Palmisano, L.; Scirè, S. Au/ TiO_2-CeO_2 catalysts for photocatalytic water splitting and vocs oxidation reactions. *Catalysts* **2016**, *6*, 121. [CrossRef]
32. Tanaka, A.; Sakaguchi, S.; Hashimoto, K.; Kominami, H. Preparation of au/TiO_2 exhibiting strong surface plasmon resonance effective for photoinduced hydrogen formation from organic and inorganic compounds under irradiation of visible light. *Catal. Sci. Technol.* **2012**, *2*, 907–909. [CrossRef]

33. Tanaka, A.; Hashimoto, K.; Kominami, H. A very simple method for the preparation of au/TiO_2 plasmonic photocatalysts working under irradiation of visible light in the range of 600–700 nm. *Chem. Commun.* **2017**, *53*, 4759–4762. [CrossRef] [PubMed]
34. Tanaka, A.; Hashimoto, K.; Kominami, H. Selective photocatalytic oxidation of aromatic alcohols to aldehydes in an aqueous suspension of gold nanoparticles supported on cerium (iv) oxide under irradiation of green light. *Chem. Commun.* **2011**, *47*, 10446–10448. [CrossRef] [PubMed]
35. Kominami, H.; Tanaka, A.; Hashimoto, K. Mineralization of organic acids in aqueous suspensions of gold nanoparticles supported on cerium (iv) oxide powder under visible light irradiation. *Chem. Commun.* **2010**, *46*, 1287–1289. [CrossRef] [PubMed]
36. Nakanishi, K.; Tanaka, A.; Hashimoto, K.; Kominami, H. Photocatalytic hydrogenation of furan to tetrahydrofuran in alcoholic suspensions of metal-loaded titanium (iv) oxide without addition of hydrogen gas. *Phys. Chem. Chem. Phys.* **2017**, *19*, 20206–20212. [CrossRef] [PubMed]
37. Tanaka, A.; Nishino, Y.; Sakaguchi, S.; Yoshikawa, T.; Imamura, K.; Hashimoto, K.; Kominami, H. Functionalization of a plasmonic au/TiO_2 photocatalyst with an ag co-catalyst for quantitative reduction of nitrobenzene to aniline in 2-propanol suspensions under irradiation of visible light. *Chem. Commun.* **2013**, *49*, 2551–2553. [CrossRef] [PubMed]
38. Sun, J.; Han, Y.; Fu, H.; Qu, X.; Xu, Z.; Zheng, S. Au@ pd/TiO_2 with atomically dispersed pd as highly active catalyst for solvent-free aerobic oxidation of benzyl alcohol. *Chem. Eng. J.* **2017**, *313*, 1–9. [CrossRef]
39. Colmenares, J.C.; Lisowski, P.; Łomot, D.; Chernyayeva, O.; Lisovytskiy, D. Sonophotodeposition of bimetallic photocatalysts pd–au/TiO_2: Application to selective oxidation of methanol to methyl formate. *ChemSusChem* **2015**, *8*, 1676–1685. [CrossRef] [PubMed]
40. Jones, W.; Su, R.; Wells, P.P.; Shen, Y.; Dimitratos, N.; Bowker, M.; Morgan, D.; Iversen, B.B.; Chutia, A.; Besenbacher, F. Optimised photocatalytic hydrogen production using core–shell aupd promoters with controlled shell thickness. *Phys. Chem. Chem. Phys.* **2014**, *16*, 26638–26644. [CrossRef] [PubMed]
41. Gallo, A.; Marelli, M.; Psaro, R.; Gombac, V.; Montini, T.; Fornasiero, P.; Pievo, R.; Santo, V.D. Bimetallic au-pt/TiO_2 photocatalysts active under uv-a and simulated sunlight for H_2 production from ethanol. *Green Chem.* **2012**, *14*, 330–333. [CrossRef]
42. Douthwaite, M.; Huang, X.; Iqbal, S.; Miedziak, P.J.; Brett, G.L.; Kondrat, S.A.; Edwards, J.K.; Sankar, M.; Knight, D.W.; Bethell, D. The controlled catalytic oxidation of furfural to furoic acid using aupd/mg (oh) 2. *Catal. Sci. Technol.* **2017**, *7*, 5284–5293. [CrossRef]
43. Redina, E.; Greish, A.; Novikov, R.; Strelkova, A.; Kirichenko, O.; Tkachenko, O.; Kapustin, G.; Sinev, I.; Kustov, L. Au/pt/TiO_2 catalysts prepared by redox method for the chemoselective 1,2-propanediol oxidation to lactic acid and an nmr spectroscopy approach for analyzing the product mixture. *Appl. Catal. A Gen.* **2015**, *491*, 170–183. [CrossRef]
44. Tan, T.H.; Scott, J.A.; Ng, Y.H.; Taylor, R.A.; Aguey-Zinsou, K.-F.; Amal, R. Plasmon enhanced selective electronic pathways in TiO_2 supported atomically ordered bimetallic au-cu alloys. *J. Catal.* **2017**, *352*, 638–648. [CrossRef]
45. Durán-Álvarez, J.C.; Avella, E.; Ramírez-Zamora, R.M.; Zanella, R. Photocatalytic degradation of ciprofloxacin using mono-(au, ag and cu) and bi-(au–ag and au–cu) metallic nanoparticles supported on TiO_2 under uv-c and simulated sunlight. *Catal. Today* **2016**, *266*, 175–187. [CrossRef]
46. Villa, A.; Jouve, A.; Sanchez Trujillo, F.J.; Motta, D.; Prati, L.; Dimitratos, N. Exploring the effect of au/pt ratio on glycerol oxidation in presence and absence of a base. *Catalysts* **2018**, *8*, 54. [CrossRef]
47. Dimitratos, N.; Porta, F.; Prati, L. Au, pd (mono and bimetallic) catalysts supported on graphite using the immobilisation method: Synthesis and catalytic testing for liquid phase oxidation of glycerol. *Appl. Catal. A Gen.* **2005**, *291*, 210–214. [CrossRef]
48. Evans, C.D.; Kondrat, S.A.; Smith, P.J.; Manning, T.D.; Miedziak, P.J.; Brett, G.L.; Armstrong, R.D.; Bartley, J.K.; Taylor, S.H.; Rosseinsky, M.J. The preparation of large surface area lanthanum based perovskite supports for aupt nanoparticles: Tuning the glycerol oxidation reaction pathway by switching the perovskite b site. *Faraday Discuss.* **2016**, *188*, 427–450. [CrossRef] [PubMed]
49. Dimitratos, N.; Lopez-Sanchez, J.A.; Anthonykutty, J.M.; Brett, G.; Carley, A.F.; Tiruvalam, R.C.; Herzing, A.A.; Kiely, C.J.; Knight, D.W.; Hutchings, G.J. Oxidation of glycerol using gold–palladium alloy-supported nanocrystals. *Phys. Chem. Chem. Phys.* **2009**, *11*, 4952–4961. [CrossRef] [PubMed]

50. Bianchi, C.L.; Canton, P.; Dimitratos, N.; Porta, F.; Prati, L. Selective oxidation of glycerol with oxygen using mono and bimetallic catalysts based on au, pd and pt metals. *Catal. Today* **2005**, *102*, 203–212. [CrossRef]
51. Dimitratos, N.; Lopez-Sanchez, J.A.; Lennon, D.; Porta, F.; Prati, L.; Villa, A. Effect of particle size on monometallic and bimetallic (au, pd)/c on the liquid phase oxidation of glycerol. *Catal. Lett.* **2006**, *108*, 147–153. [CrossRef]
52. Panagiotopoulou, P.; Karamerou, E.E.; Kondarides, D.I. Kinetics and mechanism of glycerol photo-oxidation and photo-reforming reactions in aqueous TiO_2 and pt/TiO_2 suspensions. *Catal. Today* **2013**, *209*, 91–98. [CrossRef]
53. Jedsukontorn, T.; Saito, N.; Hunsom, M. Photocatalytic behavior of metal-decorated TiO_2 and their catalytic activity for transformation of glycerol to value added compounds. *Mol. Catal.* **2017**, *432*, 160–171. [CrossRef]
54. Ning, X.; Li, Y.; Yu, H.; Peng, F.; Wang, H.; Yang, Y. Promoting role of bismuth and antimony on pt catalysts for the selective oxidation of glycerol to dihydroxyacetone. *J. Catal.* **2016**, *335*, 95–104. [CrossRef]
55. Brandner, A.; Lehnert, K.; Bienholz, A.; Lucas, M.; Claus, P. Production of biomass-derived chemicals and energy: Chemocatalytic conversions of glycerol. *Top. Catal.* **2009**, *52*, 278–287. [CrossRef]
56. Xue, W.; Wang, Z.; Liang, Y.; Xu, H.; Liu, L.; Dong, J. Promoting role of bismuth on hydrotalcite-supported platinum catalysts in aqueous phase oxidation of glycerol to dihydroxyacetone. *Catalysts* **2018**, *8*, 20. [CrossRef]
57. Porta, F.; Prati, L. Selective oxidation of glycerol to sodium glycerate with gold-on-carbon catalyst: An insight into reaction selectivity. *J. Catal.* **2004**, *224*, 397–403. [CrossRef]
58. Naldoni, A.; Riboni, F.; Marelli, M.; Bossola, F.; Ulisse, G.; Di Carlo, A.; Píš, I.; Nappini, S.; Malvestuto, M.; Dozzi, M.V. Influence of TiO_2 electronic structure and strong metal–support interaction on plasmonic au photocatalytic oxidations. *Catal.Sci. Technol.* **2016**, *6*, 3220–3229. [CrossRef]
59. Link, S.; El-Sayed, M.A. Size and temperature dependence of the plasmon absorption of colloidal gold nanoparticles. *J. Phys. Chem. B* **1999**, *103*, 4212–4217. [CrossRef]
60. De, G.; Rao, C. Au–pt alloy nanocrystals incorporated in silica films. *J. Mater. Chem.* **2005**, *15*, 891–894. [CrossRef]
61. Biesinger, M.C.; Lau, L.W.; Gerson, A.R.; Smart, R.S.C. Resolving surface chemical states in xps analysis of first row transition metals, oxides and hydroxides: Sc, ti, v, cu and zn. *Appl. Surf. Sci.* **2010**, *257*, 887–898. [CrossRef]
62. Xu, Y.; Zhang, C.; Zhang, L.; Zhang, X.; Yao, H.; Shi, J. Pd-catalyzed instant hydrogenation of TiO_2 with enhanced photocatalytic performance. *Energy Environ. Sci.* **2016**, *9*, 2410–2417. [CrossRef]
63. Gallo, A.; Montini, T.; Marelli, M.; Minguzzi, A.; Gombac, V.; Psaro, R.; Fornasiero, P.; Dal Santo, V. H_2 production by renewables photoreforming on pt–au/TiO_2 catalysts activated by reduction. *ChemSusChem* **2012**, *5*, 1800–1811. [CrossRef] [PubMed]
64. Ma, C.; Pang, G.; He, G.; Li, Y.; He, C.; Hao, Z. Layered sphere-shaped TiO_2 capped with gold nanoparticles on structural defects and their catalysis of formaldehyde oxidation. *J. Environ. Sci.* **2016**, *39*, 77–85. [CrossRef] [PubMed]
65. Boyen, H.-G.; Kästle, G.; Weigl, F.; Koslowski, B.; Dietrich, C.; Ziemann, P.; Spatz, J.P.; Riethmüller, S.; Hartmann, C.; Möller, M. Oxidation-resistant gold-55 clusters. *Science* **2002**, *297*, 1533–1536. [CrossRef] [PubMed]
66. Gao, X.; Liu, X.; Zhu, Z.; Gao, Y.; Wang, Q.; Zhu, F.; Xie, Z. Enhanced visible light photocatalytic performance of cds sensitized TiO_2 nanorod arrays decorated with au nanoparticles as electron sinks. *Sci. Rep.* **2017**, *7*, 973. [CrossRef] [PubMed]
67. Wang, Y.-Q.; Liu, Y.; Zhang, M.-X.; Min, F.-F. Electronic structure and visible-light absorption of transition metals (tm= cr, mn, fe, co) and zn-codoped srtio3: A first-principles study. *Chin. Phys. Lett.* **2018**, *35*, 017101. [CrossRef]
68. Minero, C.; Bedini, A.; Maurino, V. Glycerol as a probe molecule to uncover oxidation mechanism in photocatalysis. *Appl. Catal. B Environ.* **2012**, *128*, 135–143. [CrossRef]
69. Jedsukontorn, T.; Meeyoo, V.; Saito, N.; Hunsom, M. Effect of electron acceptors H_2O_2 and O_2 on the generated reactive oxygen species $^1O_2$ and OH in TiO_2-catalyzed photocatalytic oxidation of glycerol. *Chin. J. Catal.* **2016**, *37*, 1975–1981. [CrossRef]

70. Devarajan, S.; Bera, P.; Sampath, S. Bimetallic nanoparticles: A single step synthesis, stabilization, and characterization of au–ag, au–pd, and au–pt in sol–gel derived silicates. *J. Colloid Interface Sci.* **2005**, *290*, 117–129. [CrossRef] [PubMed]
71. Liz-Marzan, L.M.; Philipse, A.P. Stable hydrosols of metallic and bimetallic nanoparticles immobilized on imogolite fibers. *J. Phys. Chem.* **1995**, *99*, 15120–15128. [CrossRef]
72. Feng, N.; Liu, F.; Huang, M.; Zheng, A.; Wang, Q.; Chen, T.; Cao, G.; Xu, J.; Fan, J.; Deng, F. Unravelling the efficient photocatalytic activity of boron-induced Ti^{3+} species in the surface layer of TiO_2. *Sci. Rep.* **2016**, *6*, 34765. [CrossRef] [PubMed]
73. Zhao, H.; Pan, F.; Li, Y. A review on the effects of TiO_2 surface point defects on CO_2 photoreduction with H_2O. *J. Materiomics* **2017**, *3*, 17–32. [CrossRef]
74. Yi, C.-W.; Luo, K.; Wei, T.; Goodman, D. The composition and structure of pd−au surfaces. *J. Phys. Chem. B* **2005**, *109*, 18535–18540. [CrossRef] [PubMed]
75. Yu, H.; Wang, X.; Sun, H.; Huo, M. Photocatalytic degradation of malathion in aqueous solution using an au–pd–TiO_2 nanotube film. *J. Hazard. Mater.* **2010**, *184*, 753–758. [CrossRef] [PubMed]
76. Tripković, A.; Popović, K.D.; Stevanović, R.; Socha, R.; Kowal, A. Activity of a ptbi alloy in the electrochemical oxidation of formic acid. *Electrochem. Commun.* **2006**, *8*, 1492–1498. [CrossRef]
77. Zhang, L.-M.; Wang, Z.-B.; Sui, X.-L.; Li, C.-Z.; Zhao, L.; Gu, D.-M. Nitrogen-doped carbon with mesoporous structure as high surface area catalyst support for methanol oxidation reaction. *RSC Adv.* **2016**, *6*, 39310–39316. [CrossRef]
78. Cheng, H.; Huang, B.; Dai, Y.; Qin, X.; Zhang, X.; Wang, Z.; Jiang, M. Visible-light photocatalytic activity of the metastable $Bi_{20}TiO_{32}$ synthesized by a high-temperature quenching method. *J. Solid State Chem.* **2009**, *182*, 2274–2278. [CrossRef]
79. Wong, R.J.; Scott, J.; Kappen, P.; Low, G.K.-C.; Hart, J.N.; Amal, R. Enhancing bimetallic synergy with light: The effect of uv light pre-treatment on catalytic oxygen activation by bimetallic au–pt nanoparticles on a TiO_2 support. *Catal. Sci. Technol.* **2017**, *7*, 4792–4805. [CrossRef]